Contents lists available at ScienceDirect

Progress in Particle and Nuclear Physics

journal homepage: www.elsevier.com/locate/ppnp

Review

The Standard Model and Higgs physics

Ezio Torassa

INFN, Sez. di Padova, Italy

A R T I C L E   I N F O

A B S T R A C T

The Standard Model is a consistent and computable theory that successfully describes the elementary particle interactions. The strong, electromagnetic and weak interactions have been included in the theory exploiting the relation between group symmetries and group generators, in order to smartly introduce the force carriers. The group properties lead to constraints between boson masses and couplings. All the measurements performed at the LEP, Tevatron, LHC and other accelerators proved the consistency of the Standard Model. A key element of the theory is the Higgs field, which together with the spontaneous symmetry breaking, gives mass to the vector bosons and to the fermions. Unlike the case of vector bosons, the theory does not provide prediction for the Higgs boson mass. The LEP experiments, while providing very precise measurements of the Standard Model theory, searched for the evidence of the Higgs boson until the year 2000. The discovery of the top quark in 1994 by the Tevatron experiments and of the Higgs boson in 2012 by the LHC experiments were considered as the completion of the fundamental particles list of the Standard Model theory. Nevertheless the neutrino oscillations, the dark matter and the baryon asymmetry in the Universe evidence that we need a new extended model. In the Standard Model there are also some unattractive theoretical aspects like the divergent loop corrections to the Higgs boson mass and the very small Yukawa couplings needed to describe the neutrino masses. For all these reasons, the hunt of discrepancies between Standard Model and data is still going on with the aim to finally describe the new extended theory.

Contents

E-mail address: ezio.torassa@pd.infn.it.

1. Introduction

1.1. Electroweak history

The weak interaction was discovered by Antoine Henry Becquerel in 1896 [1] when he found that a nucleus may decay into a different nucleus plus a β ray. Wolfgang Pauli in 1930 [2] postulated the existence of a new particle, the neutrino, to make possible the momentum and energy conservation despite the continuous distribution of energy of the β particles. Subsequently, in 1932, the neutron was discovered by James Chadwick [3] and the decay of a nucleus was interpreted as the decay of a neutron inside the nucleus:

$$n \rightarrow p + e^- + \overline{\nu}_e \tag{1}$$

The description of the weak interactions was proposed by Enrico Fermi in 1934 [4]. Fermi assumed that the emission of a electron–neutrino pair was analogous to the electromagnetic emission of a photon. Since the electromagnetic interaction of a charged particle is given by:

$$\mathcal{L}_{\text{e.m.}} = eA_\mu \overline{\psi} \gamma^\mu \psi \tag{2}$$

where ψ is the field describing the charged particles, A_μ the electromagnetic field and $\overline{\psi} = \psi^\dagger \gamma^0$, the Fermi ansatz for the Lagrangian of the neutron decay was:

$$\mathcal{L}_{\text{weak}} = G_F (\overline{\psi}_e \gamma_\mu \psi_\nu)(\overline{\psi}_p \gamma^\mu \psi_n) \tag{3}$$

where G_F is the Fermi coupling constant. The main problem of the Fermi theory is its non-renormalizability. The renormalizability rule for a theory is to have positive dimensions in mass for every coupling:

$$[g_i] \geq 0 \quad \text{for any } i \tag{4}$$

The dimensions of $\mathcal{L}, \psi, A_\mu$ in natural units ($L = T = M^{-1}$) are:

$$[\mathcal{L}] = 4 \quad [\psi] = 3/2 \quad [A_\mu] = 1 \tag{5}$$

the resulting dimension for e in Eq. (2) is 0, for G_F in Eq. (3) is -2. The problem can be solved introducing an intermediate vector boson. The idea was proposed by Julian Schwinger in 1957 [5] and extended to a neutral vector boson by Sidney Bludman in 1958 [6] and Sheldon Glashow in 1961 [7] deriving the Fermi interaction from the SU(2) symmetry. The description of the electroweak theory including the electromagnetic and weak interactions is due to Sheldon Glashow, Steven Weinberg and Abdus Salam [7–9].

1.2. Scope and content of the review

Several textbooks [10–13] and reviews [14–17] on the Standard Model and Higgs physics are available in the scientific literature. There are usually differences in the notation used for the theoretical introductions. The aim is to learn from the previous descriptions and try to improve the didactic aspects. The most recent results are reported but due to the wide subject a selection is needed. The Standard Model and the mechanism of electroweak symmetry breaking are described in Section 2. The historical Higgs boson searches at LEP and Tevatron are reported in Sections 3.2 and 4.3 including the last Tevatron combination. The discovery of the Higgs boson at LHC, the most recent measurements of the Higgs boson properties at LHC and the global electroweak fit are reported in Sections 4.4, 4.5 and 7. The physics perspectives for the precise Higgs boson characterization at the future colliders are described in Sections 3.3 and 6.

2. The standard model and the Higgs boson

2.1. Global and local gauge symmetries

A symmetry is global if it holds for every space–time point. Considering the Lagrangian density of a Dirac field:

$$\mathcal{L} = \overline{\psi}(x)(i\partial_\mu \gamma^\mu - m)\psi(x) \tag{6}$$

for a phase change $\psi(x) \rightarrow e^{i\alpha}\psi(x)$ the equation is invariant for every point, this is called global symmetry. The first Noether's theorem states that global symmetries lead to continuity equations $\partial_\mu j_k^\mu = 0$ and thereby to conserved charges (subject to suitable boundary conditions). If the phase change is space–time dependent the equation is not invariant for every point due to the presence of derivatives:

$$\psi(x) \rightarrow e^{i\alpha(x)}\psi(x) \qquad \partial_\mu(e^{i\alpha(x)}\psi(x)) = e^{i\alpha(x)}(\partial_\mu \psi(x) + i\partial_\mu \alpha(x)\,\psi(x)) \tag{7}$$

In order to make Eq. (6) invariant under local phase transformations, one may consider the addition of new terms whose variation will compensate for the $\partial_\mu \alpha(x)$ term like a modified derivative D_μ transforming according to:

$$D_\mu \psi(x) \rightarrow e^{i\alpha(x)} D_\mu \psi(x) \tag{8}$$

Including in the Dirac equation the following modified derivative:

$$D_\mu = \partial_\mu - iqB_\mu \qquad \overline{\psi}(iD_\mu \gamma^\mu - m)\psi \tag{9}$$

the equation becomes invariant under local phase change if a gauge transformation is applied to the new field:

$$B_\mu \rightarrow B_\mu + \frac{1}{q}\partial_\mu \alpha(x) \tag{10}$$

The second Noether's theorem states that local symmetries lead to relations between the Lagrangian and their derivatives. These relations are called Noether identities and are related to the gauge transformations.

2.2. The gauge structure of the standard model

The Glashow–Weinberg–Salam electroweak theory [7–9] which describes the electromagnetic and weak interactions between quarks and leptons, is based on the symmetry group $SU(2)_L \times U(1)_Y$. The QCD theory [18,19], is based on the symmetry group $SU(3)_C$. Before the electroweak symmetry breaking, the *SM* is a theory with massless bosons and invariant under local transformations represented by elements of the symmetry group $SU(2)_L \times U(1)_Y \times SU(3)_C$.

2.3. The Lagrangian of the standard model

The matter fields are the quarks and lepton fermions with their left-handed and the right-handed components. The left-handed fermions are in weak isotopic doublets, while the right-handed are in weak isotopic singlets. The neutrinos are considered massless and appear only with their left-handed components:

$$
\begin{aligned}
L_1 &= \begin{pmatrix} \nu_e \\ e^- \end{pmatrix}_L, & l_{R_1} &= e_R^-, & Q_1 &= \begin{pmatrix} u \\ d \end{pmatrix}_L, & u_{R_1} &= u_R, & d_{R_1} &= d_R, \\
L_2 &= \begin{pmatrix} \nu_\mu \\ \mu^- \end{pmatrix}_L, & l_{R_2} &= \mu_R^-, & Q_2 &= \begin{pmatrix} c \\ s \end{pmatrix}_L, & u_{R_2} &= c_R, & d_{R_2} &= s_R, \\
L_3 &= \begin{pmatrix} \nu_\tau \\ \tau^- \end{pmatrix}_L, & l_{R_3} &= \tau_R^-, & Q_3 &= \begin{pmatrix} t \\ b \end{pmatrix}_L, & u_{R_3} &= t_R, & d_{R_3} &= b_R.
\end{aligned}
\tag{11}
$$

The generation of SU(2) elements is usually described with the Pauli matrices:

$$g \in \mathrm{SU}(2) = e^{i(\alpha_1\sigma_1+\alpha_2\sigma_2+\alpha_3\sigma_3)}, \quad \sigma_1 = \begin{pmatrix} 0 & 1 \\ 1 & 0 \end{pmatrix}, \quad \sigma_2 = \begin{pmatrix} 0 & -i \\ i & 0 \end{pmatrix}, \quad \sigma_3 = \begin{pmatrix} 1 & 0 \\ 0 & -1 \end{pmatrix} \tag{12}$$

The weak isospin is defined as $I_f^i = \frac{1}{2}\sigma_i$ in analogy with the spin, it is not a spin but the same mathematics is used to describe the symmetry between two quantum states. The third component of the weak isospin I_f^3 is zero acting on singlets, $+\frac{1}{2}$ and $-\frac{1}{2}$ acting on the up and down elements of the doublets. The fermion hypercharge Y_f is the one-dimension matrix representing the generator of the $\mathrm{U}(1)_Y$ group:

$$g \in \mathrm{U}(1) = e^{i\alpha Y_f}. \tag{13}$$

Eigenvalues of the weak isospin are constrained by the $\mathrm{SU}(2)_L$ structure but the eigenvalue of the hypercharge is a free parameter. Only after the electric charge Q_f is derived in terms of I_3^f and Y_f the value of the hypercharge acting on fermions is assigned.

$$Y_f = 2(Q_f - I_f^3) \;\Rightarrow\; Y_{L_i} = -1, \; Y_{l_{R_i}} = -2, \; Y_{Q_i} = \frac{1}{3}, \; Y_{u_{R_i}} = \frac{4}{3}, \; Y_{d_{R_i}} = -\frac{2}{3}. \tag{14}$$

Consider the QED Lagrangian:

$$\mathcal{L}_{QED} = -\frac{1}{4}F_{\mu\nu}F^{\mu\nu} + \overline{\psi}(i\partial_\mu\gamma^\mu - m)\psi \tag{15}$$

This Lagrangian is invariant under global U(1) transformation but not local. Replacing the 4-gradient ∂_μ with $D_\mu = \partial_\mu - ig'Y_q B_\mu$ the Lagrangian becomes gauge invariant that means invariant under local phase rotations with simultaneous shifts of the gauge field:

$$\psi(x) \to e^{iY_q\alpha(x)}, \; B_\mu \to B_\mu + \frac{1}{g'}\partial_\mu\alpha(x) \tag{16}$$

The requirement of the gauge $\mathrm{SU}(2)_L \times \mathrm{U}(1)_Y \times \mathrm{SU}(3)_C$ symmetry requires the introduction of:

- three $W_\mu^{1,2,3}$ fields (with the $I^{1,2,3}$ generators of the SU(2) group and the coupling strength g);
- a single B_μ field (with the Y generator of the U(1) group and the coupling strength g');
- eight $G_\mu^{1,\dots,8}$ fields (with the $T^{1,\dots,8}$ generators of the SU(3) group and the coupling strength g_S);

and consequently accommodate the presence of three weak, one electromagnetic and eight strong mediators.

The Lagrangian $\mathcal{L}_{SM}$ of the *SM* can be divided into four different parts,

$$\mathcal{L}_{SM} = \mathcal{L}_{YM} + \mathcal{L}_{ferm} + \mathcal{L}_H + \mathcal{L}_{Yuk} \tag{17}$$

which will be discussed in the following. The Yang–Mills part $\mathcal{L}_{YM}$ describes the dynamics of the gauge bosons, i.e. their free propagation as well as their self-interactions,

$$\mathcal{L}_{YM} = -\frac{1}{4}W_{\mu\nu}^i W^{i,\mu\nu} - \frac{1}{4}B_{\mu\nu}B^{\mu\nu} - \frac{1}{4}G_{\mu\nu}^a G^{a,\mu\nu}, \tag{18}$$

where

$$\begin{aligned}
W_{\mu\nu}^i &= \partial_\mu W_\nu^i - \partial_\nu W_\mu^i + g\epsilon^{ijk}W_\mu^j W_\nu^k, \qquad i,j,k = 1,2,3, \\
B_{\mu\nu} &= \partial_\mu B_\nu - \partial_\nu B_\mu, \\
G_{\mu\nu}^a &= \partial_\mu G_\nu^a - \partial_\nu G_\mu^a + g_s f^{abc}G_\mu^b G_\nu^c, \qquad a,b,c = 1,\dots,8.
\end{aligned} \tag{19}$$

Naive gauge-boson mass terms, such as $-m^2\, W_\mu^i W^{i,\mu}$ for the W bosons cannot be introduced in the Lagrangian because they violate the gauge invariance.

The fermion part $\mathcal{L}_{ferm}$ is the Dirac Lagrangian with the modified 4-gradient and without the mass term:

$$\mathcal{L}_{ferm} = \overline{\psi}(iD_\mu\gamma^\mu)\psi + h.c. \tag{20}$$

where:

$$D_\mu = \partial_\mu - igI_f^i W_\mu^i - ig'\frac{Y_f}{2}B_\mu - ig_s T_f^a G_\mu^a. \tag{21}$$

The part with I_f^i is not present for right-handed fermions and the part with T_f^a is not present for leptons. The mass term $-m\overline{\psi}\psi$ is not allowed in the Lagrangian because is not gauge invariant. This is clear considering e.g. leptons and decomposing the expression in helicity states:

$$-m\overline{\psi}\psi = -m[\overline{\psi}_R\psi_L + \overline{\psi}_L\psi_R] \tag{22}$$

but ψ_L and ψ_R transforms differently:

$$\psi_L \rightarrow e^{i\alpha Y + i\beta I} \psi_L \qquad \psi_R \rightarrow e^{i\alpha Y} \psi_R \, . \tag{23}$$

The *SM* Lagrangian without the mass term for fermions and gauge bosons contains only the Yang–Mills and the fermion parts:

$$\begin{aligned}
\mathcal{L}_{\text{YM}} + \mathcal{L}_{\text{ferm}} = &- \frac{1}{4} W_{\mu\nu}^i W^{i,\mu\nu} - \frac{1}{4} B_{\mu\nu} B^{\mu\nu} - \frac{1}{4} G_{\mu\nu}^a G^{a,\mu\nu} \\
&+ \bar{L}_i i D_\mu \gamma^\mu L_i + \bar{l}_{Ri} i D_\mu \gamma^\mu l_{Ri} + \bar{Q}_i i D_\mu \gamma^\mu Q_i + \bar{u}_{Ri} i D_\mu \gamma^\mu u_{Ri} + \bar{d}_{Ri} i D_\mu \gamma^\mu d_{Ri} \, .
\end{aligned} \tag{24}$$

The introduction of particle masses requires the extension of the theory.

2.4. Spontaneous symmetry breaking

To understand the symmetry breaking mechanism the simplest example with a single complex scalar field $\phi(x)$ can be considered. The Lagrangian density is:

$$\mathcal{L} = (\partial_\mu \phi)^\dagger (\partial_\mu \phi) - V(\phi). \tag{25}$$

The $V(\phi)$ potential with the renormalizability assumption is:

$$V(\phi) = a \, \phi^\dagger \phi + b \, (\phi^\dagger \phi)^2 \tag{26}$$

The ground state of the field is the minimum of the potential. The b coefficient should be real and positive to have a real potential with a minimum value. The position and type of the minimum depends on the sign of a. For $a > 0$ the potential has the form of a parabola (Fig. 1 left) and there is a single minimum. The unique minimum of the parabola is $\phi = 0$ and it shares the U(1) symmetry of the Lagrangian. For $a < 0$ the potential has the shape of a Mexican hat (Fig. 1 right), there is not a unique ground state for this system but a set of degenerate vacuum states lying on a ring in the complex plane. Each ground state is asymmetric under the U(1) symmetry of the Lagrangian. Applying the U(1) transformation to any of the vacuum states will rotate it to a different orientation that describes a different physical state. Now we express the $\phi(x)$ field with small perturbations around one ground state. We choose e.g. the state in the positive real axis:

$$\phi(x) = (v + \eta(x)) e^{i\xi(x)} \tag{27}$$

The $\eta(x)$ and $\xi(x)$ functions represents real fields. We rewrite the potential like the following :

$$V(\phi) = -\mu^2 \phi^\dagger \phi + \lambda (\phi^\dagger \phi)^2 \tag{28}$$

Considering real μ we are in the condition previously described with negative a. The minimum of the potential v can be derived as a function of the λ and μ parameters:

$$v = \sqrt{\frac{\mu^2}{2\lambda}} \quad \text{or} \quad \mu^2 = 2\lambda v^2 \tag{29}$$

For non zero ground states the Lagrangian shows a mass term for the new field $\eta(x)$:

$$\begin{aligned}
\mathcal{L} &= \partial_\mu \eta \partial_\mu \eta + (v + \eta)^2 \partial_\mu \xi \partial_\mu \xi + \mu^2 (v + \eta)^2 - \lambda (v + \eta)^4 \\
&= \partial_\mu \eta \partial_\mu \eta + (v + \eta)^2 \partial_\mu \xi \partial_\mu \xi - 4\lambda v^2 \eta^2 + \text{higher order}
\end{aligned} \tag{30}$$

The first order term $\eta(x)$ deriving from the quadratic and fourth order terms in Eq. (30) are canceled due to the vacuum state Eq. (29). The mass of the $\eta(x)$ field is $m_\eta^2 = 4\lambda v^2$. The $\xi(x)$ field is a massless boson also called Goldstone boson. The presence of a massless boson for each broken global symmetry is formulated in the Goldstone theorem [20,21]. We started with a Lagrangian invariant under U(1), the new Lagrangian expressed in term of small oscillation around a specific vacuum state is not invariant anymore under U(1). The invariance has been broken due to the presence of not invariant vacuum states. This mechanism is called "spontaneous symmetry breaking".

2.5. Electroweak symmetry breaking

A historical milestone in this development of the *SM* was laid with the realization that a spontaneous breaking of the gauge symmetry, driven by a self-interacting scalar field, can lend mass to gauge bosons [22–25]. This idea is known as the Brout–Englert–Higgs–Guralnik–Hagen–Kibble (BEHGHK) or the Brout–Englert–Higgs (BEH) mechanism, simply the "Higgs mechanism". Starting from the SU(2)$_L$ × U(1)$_Y$ × SU(3)$_C$ invariant Lagrangian of the Standard Model with massless bosons we must give mass to the W^+, W^- and Z^0 bosons and let the photon massless. It is clear that we need at least 3 additional degrees of freedom. We consider a doublet of charged scalar field having 4 degrees of freedom:

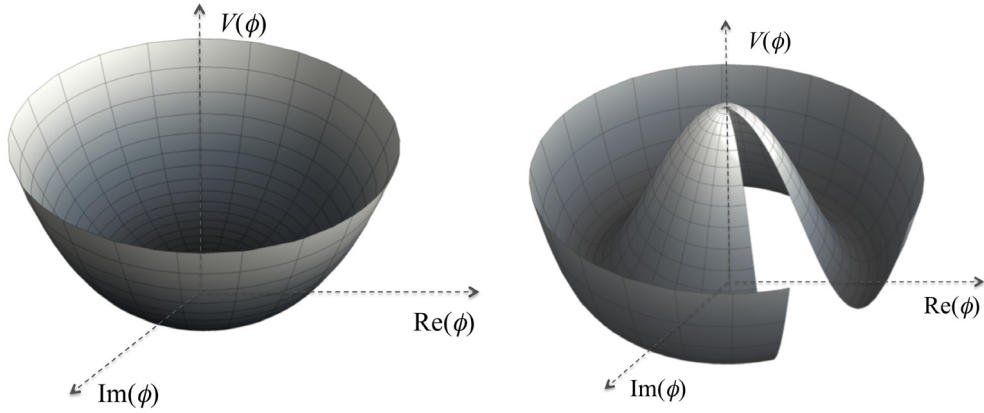$$\Phi = \begin{pmatrix} \phi^+ \\ \phi^0 \end{pmatrix} . \tag{31}$$

Fig. 1. Potential $V(\phi)$ for $a > 0$ (left) and $a < 0$ (right).

The part of the *SM* equation with the Higgs field (Eq. (17)) can be expressed extending the Lagrangian described in the previous section (Eq. (25))

$$\mathcal{L}_H = (D_\mu \Phi)^\dagger (D^\mu \Phi) - V(\Phi). \tag{32}$$

The self-interaction of Φ is described by the potential

$$V(\Phi) = -\mu^2 (\Phi^\dagger \Phi) + \lambda (\Phi^\dagger \Phi)^2. \tag{33}$$

Requiring that the vacuum expectation value (vev) is electrically neutral, forces the upper component of Φ_0 to vanish, i.e. Φ_0 is fixed up to a phase, with the usual choice:

$$\Phi_0 = \frac{1}{\sqrt{2}} \begin{pmatrix} 0 \\ v \end{pmatrix}, \qquad v = \sqrt{\frac{\mu^2}{\lambda}}. \tag{34}$$

This freedom in choosing the vev Φ_0 of Φ reflects the spontaneous breakdown of the SU(2)$_L$ × U(1)$_Y$ symmetry. Splitting off the vev from Φ,

$$\Phi = \frac{1}{\sqrt{2}} \begin{pmatrix} \eta_1 + i\eta_2 \\ v + H + i\eta_3 \end{pmatrix}, \tag{35}$$

we reparameterize Φ in terms of the real physical Higgs field H and the unphysical Goldstone boson fields η_1, η_2 and η_3. With the appropriate choice of the gauge the unphysical η fields vanish:

$$\Phi(x) \to e^{-i\theta_a(x)\tau^a(x)} \Phi(x) = \frac{1}{\sqrt{2}} \begin{pmatrix} 0 \\ v + H \end{pmatrix}. \tag{36}$$

In the covariant derivative (Eq. (21)) we set the conditions $I_f^i = \sigma^i/2$, $Y_f = 1$ and $T_f^a = 0$ then making use of this gauge we expand the term $|D_\mu \Phi|^2$:

$$|D_\mu \Phi|^2 = \frac{1}{2}(\partial H)^2 + \frac{1}{8}g^2(v + H)^2 |W_\mu^1 + iW_\mu^2|^2 + \frac{1}{8}(v + H)^2 |gW_\mu^3 - g'B_\mu|^2 \tag{37}$$

we define the new fields $W_\mu^\pm$, Z_μ and A_μ:

$$W_\mu^\pm = \frac{1}{\sqrt{2}}(W_\mu^1 \mp iW_\mu^2), \qquad Z_\mu = \frac{gW_\mu^3 - g'B_\mu}{\sqrt{g^2 + g'^2}}, \qquad A_\mu = \frac{g'W_\mu^3 + gB_\mu}{\sqrt{g^2 + g'^2}}. \tag{38}$$

The part of the *SM* equation with the Higgs field in this gauge becomes:

$$\mathcal{L}_{H,U\text{-gauge}} = \frac{1}{2}(\partial H)^2 + \frac{g^2}{4}(v + H)^2 W_\mu^+ W^{-\mu} + \frac{(g^2 + g'^2)}{8}(v + H)^2 Z_\mu Z^\mu + \frac{\mu^2}{2}(v + H)^2 - \frac{\lambda}{4}(v + H)^4. \tag{39}$$

Massive bosons should have the following bilinear terms:

$$M_W^2 W_\mu^+ W^{-\mu}, \qquad \frac{1}{2}M_Z^2 Z_\mu Z^\mu, \qquad \frac{1}{2}M_A^2 A_\mu A^\mu. \tag{40}$$

From Eq. (39) the boson masses are:

$$M_W = \frac{1}{2}vg, \quad M_Z = \frac{1}{2}v\sqrt{g^2 + g'^2}, \quad M_A = 0. \tag{41}$$

Now we consider the part of the Lagrangian with the standalone Higgs field. The first order of the H field has two contributions: $\mu^2 vH$ from the $\frac{\mu^2}{2}(v - H)^2$ term and $-\lambda v^3 H$ from the $\frac{\lambda}{2}(v - H)^4$ term. These contributions cancel out due the relation $\mu^2 = v^2\lambda$. The second order of the H field has three contributions, their sum gives $-\mu^2 H^2$. Considering the Lagrangian density for scalar fields $\frac{1}{2}(\partial\phi)^2 - \frac{1}{2}m^2\phi^2$ the Higgs boson mass is:

$$M_H = \sqrt{2\mu^2} \tag{42}$$

In the Lagrangian density the parameters μ^2, λ and v can be replaced with the masses defined in Eqs. (41) and (42):

$$\begin{aligned}
\mathcal{L}_{H,U\text{-gauge}} &= \frac{1}{2}(\partial H)^2 - \frac{1}{2}M_H^2 H^2 + M_W^2 W_\mu^+ W^{-,\mu} + \frac{1}{2}M_Z^2 Z_\mu Z^\mu \\
&\quad + gM_W HW_\mu^+ W^{-\mu} + \frac{g^2}{4}H^2 W_\mu^+ W^{-\mu} + \frac{gM_Z}{2c_w}HZ_\mu Z^\mu + \frac{g^2}{4c_w^2}H^2 Z_\mu Z^\mu \\
&\quad - \frac{gM_H^2}{4M_W}H^3 - \frac{g^2 M_H^2}{32M_W^2}H^4 + \text{const.},
\end{aligned} \tag{43}$$

where $c_w = \cos\theta_W = g/\sqrt{g^2 + g'^2} = M_W/M_Z$ and consequently $s_w = \sin\theta_W = g'/\sqrt{g^2 + g'^2}$. Considering the mixing matrix of the neutral bosons:

$$\begin{pmatrix} Z_\mu \\ A_\mu \end{pmatrix} = \begin{pmatrix} c_w & -s_w \\ s_w & c_w \end{pmatrix} \begin{pmatrix} W_\mu^3 \\ B_\mu \end{pmatrix}, \tag{44}$$

the couplings between the neutral vector bosons and the fermions are transformed from g (W_μ^3) and g' (B_μ) to $c_w g - s_w g'$ (Z_μ) and $s_w g + c_w g'$ (A_μ). The last is the coupling constant $e = gg'/\sqrt{g^2 + g'^2}$. The minimum of the Higgs potential v is usually called vacuum expectation value (v.e.v.) despite the factor $\sqrt{2}$ in the relation between Φ_0 and v (Eq. (34)). From the equation of the M_W mass (Eq. (41)) we can estimate v:

$$v = \frac{2M_W}{g} = \frac{2M_W s_w}{e} = \frac{2M_W s_w}{\sqrt{4\pi\alpha}} \simeq 247 \text{ GeV} \tag{45}$$

2.6. The couplings of the Higgs boson to the vector bosons

The couplings of the Higgs boson to the vector bosons g_{HWW} and g_{HZZ} are the multiplication factors of the $HW_\mu^+ W^{-\mu}$ and $HZ_\mu Z^\mu$ term in the Eq. (43):

$$g_{HWW} = gM_W = \frac{2M_W^2}{v} \qquad g_{HZZ} = \frac{g\,M_Z}{2c_W} = \frac{M_Z^2}{v} \qquad g_{HVV} = \frac{2M_V^2}{v}S_{VV} \tag{46}$$

where $S_{WW} = 1$ and $S_{ZZ} = \frac{1}{2}$.

2.7. The Higgs boson predictions

Before the Higgs boson discovery, the *SM* made the following phenomenological predictions:

- the Higgs field H implies the existence of a neutral spinless particle, the mass of this boson is a free parameter of the model ($M_H = \sqrt{2\mu^2}$);
- the weak-gauge-boson masses are related to the gauge couplings: $c_w = M_W/M_Z$;
- the couplings of the Higgs boson to the massive gauge bosons ($HV^\dagger V$) are proportional to the gauge coupling g and to the mass of the bosons M_V (or to the ratio $\frac{M_V^2}{v}$);
- the triple (H^3) and quartic (H^4) Higgs boson self interactions are predicted and are both proportional to M_H^2.

The Higgs boson predicted from the spontaneous symmetry breaking mechanism is considered an excited state of the vacuum and it should carry the same quantum numbers. The vacuum has no charge and is invariant under parity, the expected quantum numbers of the Higgs boson are $J^{PC} = 0^{++}$.

2.8. Yukawa couplings and fermion masses

Dirac mass terms like Eq. (22) are forbidden by the $SU(2)_L \times U(1)_Y$ symmetry because they mix the left and right-handed components of the fermion fields, which transform differently under the *SM* gauge group. However the new scalar field

allows writing gauge-invariant fermion–scalar couplings:

$$\mathcal{L}_{\text{Yuk}} = -G[\overline{\psi}_L \Phi \psi_R + \overline{\psi}_R \Phi^\dagger \psi_L]. \tag{47}$$

We express the scalar field with small oscillation around the vacuum in the U-gauge like in Eq. (36). The electron contribution to the Yukawa Lagrangian is:

$$
\begin{aligned}
\mathcal{L}_e &= -G_e \frac{1}{\sqrt{2}} \Big[(\overline{v}, \overline{e})_L \begin{pmatrix} 0 \\ v+H \end{pmatrix} e_R + \overline{e}_R(0,\, v+H) \begin{pmatrix} v \\ e \end{pmatrix}_L \Big] \\
&= -G_e \frac{(v+H)}{\sqrt{2}} [\overline{e}_L e_R + \overline{e}_R e_L] \\
&= -G_e \frac{(v+H)}{\sqrt{2}} \overline{e}e \\
&= \quad -\frac{G_e v}{\sqrt{2}} \overline{e}e \qquad -\frac{G_e}{\sqrt{2}} H\overline{e}e \\
&\quad\ \ \text{electron mass} \quad \text{electron–Higgs field interaction}
\end{aligned}
\tag{48}
$$

The Yukawa mass term is analogous to the Dirac mass term with the identity $m_e = \frac{G_e v}{\sqrt{2}}$, generalizing for different interactions and different fermions:

$$m_f = \frac{G_f v}{\sqrt{2}} = g_{Hff}\ v \tag{49}$$

The inverted relation is another phenomenological prediction: the interactions between the Higgs field and fermions are proportional to the fermions masses. Thus, the $H\overline{f}f$ coupling is uniquely predicted in the *SM* once the fermion mass and v are known. The coupling of the Higgs boson to electrons is very small compared to the coupling of the Higgs boson to tau leptons:

$$g_{Hee} = \frac{m_e}{v} = \frac{511\ \text{keV}}{247\ \text{GeV}} \simeq 2.1\ 10^{-6} \qquad g_{H\tau\tau} = \frac{m_\tau}{v} = \frac{1.78\ \text{GeV}}{247\ \text{GeV}} \simeq 7.2\ 10^{-3} \tag{50}$$

The *SM* does not provide any explanation for these numbers or their sizes.

2.9. The CKM matrix

The Yukawa term in Eq. (47) can give mass only to the "down" type of the fermion doublets. The charge conjugate of the Higgs field can solve the problem because it flips the "up" with the "down" sectors:

$$\Phi^c = \begin{pmatrix} \phi^+ \\ \phi^0 \end{pmatrix}^c = i\sigma_2 \Phi^* = \begin{pmatrix} (\phi^0)^* \\ -\phi^- \end{pmatrix}^c \tag{51}$$

For small oscillations around the vacuum we find:

$$\Phi^c = \frac{1}{\sqrt{2}} \begin{pmatrix} v+H \\ 0 \end{pmatrix} \tag{52}$$

With the same procedure of Eq. (48) we can get masses for the "up" component of doublets. Using the notation introduced in Section 2.3 and considering massless neutrinos, the general Yukawa coupling contribution to the Lagrangian is:

$$\mathcal{L}_{\text{Yuk}} = -G^l_{i,j} \overline{L}_i \Phi l_{Rj} - G^u_{i,j} \overline{Q}_i \Phi^c u_{Rj} - G^d_{i,j} \overline{Q}_i \Phi d_{Rj} + \text{h.c.}, \tag{53}$$

where "h.c." means hermitian conjugate. The symbols $G^l_{i,j}$, $G^u_{i,j}$, $G^d_{i,j}$ represent arbitrary complex 3×3 matrices. After symmetry breaking, considering only the quark terms and omitting the $H\overline{q}q$ interaction terms the Lagrangian becomes:

$$\mathcal{L}^{\text{quarks}}_{\text{Yuk}} = -G^u_{i,j} \overline{u}_{Li} \frac{v}{\sqrt{2}} u_{Rj} - G^d_{i,j} \overline{d}_{Li} \frac{v}{\sqrt{2}} d_{Rj} + \text{h.c.} \tag{54}$$

The mass matrices are introduced in relation with the coupling matrices:

$$M^u_{i,j} = \frac{G^u_{i,j} v}{\sqrt{2}}, \qquad M^d_{i,j} = \frac{G^d_{i,j} v}{\sqrt{2}} \tag{55}$$

$$-\mathcal{L}^{\text{quarks}}_{\text{Yuk}} = M^u_{i,j} \overline{u}_{Li} u_{Rj} + M^d_{i,j} \overline{d}_{Li} d_{Rj} + \text{h.c.} \tag{56}$$

The non-diagonal term of the mass matrices mix the left- and right-handed parts of different generation of quarks. The fermion fields in the Lagrangian are supposed to be in the interaction (flavor) basis. Owing to the mixing terms, a fermion

of flavor f_i ($i = 1, 2, 3$) of the ith generation can oscillate into f_j of the other generations even during a free propagation in space and time. This oscillation can be removed upon transforming the fields from the "flavor basis" into a "mass basis". To obtain the mass eigenstates the mass matrices M^d and M^u must be diagonalized with unitary matrices V_L^d, V_R^d, V_L^u and V_R^u:

$$-\mathcal{L}_{\text{Yuk}}^{\text{quarks}} = \overline{u}_{Li} (V_L^{u\dagger} V_L^u) M_{i,j}^u (V_R^{u\dagger} V_R^u) u_{Rj} + \overline{d}_{Li} (V_L^{d\dagger} V_L^d) M_{i,j}^d (V_R^{d\dagger} V_R^d) d_{Rj} + \text{h.c.}$$
$$= \overline{u_{Li}^{\text{mass}}} (V_L^u M_{i,j}^u V_R^{u\dagger}) u_{Rj}^{\text{mass}} + \overline{d_{Li}^{\text{mass}}} (V_L^d M_{i,j}^d V_R^{d\dagger}) d_{Rj}^{\text{mass}} + \text{h.c.} \quad (57)$$
$$= \overline{u_{Li}^{\text{mass}}} (M_{i,j}^u)_{\text{diag}} u_{Rj}^{\text{mass}} + \overline{d_{Li}^{\text{mass}}} (M_{i,j}^d)_{\text{diag}} d_{Rj}^{\text{mass}} + \text{h.c.} ,$$

where

$$M_{\text{diag}}^u = V_L^u M^u V_R^{u\dagger} \quad \text{and} \quad M_{\text{diag}}^d = V_L^d M^d V_R^{d\dagger} . \quad (58)$$

The fermion part of the Lagrangian in Eq. (24) has the following quarks term:

$$\mathcal{L}_{\text{ferm}}^{\text{quarks}} = \overline{Q}_i i D_\mu \gamma^\mu Q_i + \overline{u}_{Ri} i D_\mu \gamma^\mu u_{Ri} + \overline{d}_{Ri} i D_\mu \gamma^\mu d_{Ri} \quad (59)$$

For this Lagrangian express the quark fields into the mass basis. The right-handed component of quarks do not have weak interactions and for them the V matrices cancel out:

$$\overline{u}_{Ri} i D_\mu \gamma^\mu u_{Ri} = \overline{u_{Rk}^{\text{mass}}} (V_R^u)_{ik} i (\partial_\mu - ig' \frac{Y_f}{2}) \gamma^\mu (V_R^{u\dagger})_{ij} u_{Rj}^{\text{mass}} = \overline{u_{Ri}^{\text{mass}}} i D_\mu \gamma^\mu u_{Ri}^{\text{mass}} \quad (60)$$

The weak interaction for left-handed quarks is:

$$\mathcal{L}_{\text{ferm}}^{\text{L-quarks}} = \overline{Q}_i i (\partial_\mu - ig \frac{\vec{\sigma}}{2} \vec{W}_\mu) \gamma^\mu Q_i$$
$$= \overline{(u \ d)}_{Li} i (\partial_\mu - ig \frac{\vec{\sigma}}{2} \vec{W}_\mu) \gamma^\mu \begin{pmatrix} u \\ d \end{pmatrix}_{Li}$$
$$= \frac{g}{\sqrt{2}} \overline{u_{Li}} \gamma_\mu W^{-\mu} d_{Li} + \frac{g}{\sqrt{2}} \overline{d_{Li}} \gamma_\mu W^{+\mu} u_{Li} + \cdots \quad (61)$$
$$= \frac{g}{\sqrt{2}} \overline{u_{Lk}^{\text{mass}}} (V_L^u V_L^{d\dagger})_{kj} \gamma_\mu W^{-\mu} d_{Lj}^{\text{mass}} + \frac{g}{\sqrt{2}} \overline{d_{Lk}^{\text{mass}}} (V_L^d V_L^{u\dagger})_{kj} \gamma_\mu W^{+\mu} u_{Lj}^{\text{mass}} + \cdots$$

where $W^{\pm\mu}$ are the fields already defined in Eq. (38). The combination $(V_L^d V_L^{u\dagger})_{kj} = (V_L^u V_L^{d\dagger})_{kj}^\dagger$ is the unitary matrix known with the name of Cabibbo–Kobayashi–Maskawa (CKM) mixing matrix:

$$V_{\text{CKM}} = V_L^d V_L^{u\dagger}. \quad (62)$$

By convention the interaction eigenstates and the mass eigenstates are chosen to be equal for the up-type quarks and rotated for the down-type quarks:

$$\begin{pmatrix} u \\ c \\ t \end{pmatrix} = \begin{pmatrix} u^{\text{mass}} \\ c^{\text{mass}} \\ t^{\text{mass}} \end{pmatrix} \qquad \begin{pmatrix} d \\ s \\ b \end{pmatrix} = \begin{pmatrix} V_{ud} & V_{us} & V_{ub} \\ V_{cd} & V_{cs} & V_{cb} \\ V_{td} & V_{ts} & V_{tb} \end{pmatrix} \begin{pmatrix} d^{\text{mass}} \\ s^{\text{mass}} \\ b^{\text{mass}} \end{pmatrix} \quad (63)$$

2.10. The PMNS matrix

The Pontecorvo–Maki–Nakagawa–Sakata matrix describes the rotation between mass and interaction eigenstates is in the lepton sector. The weak interaction for the left-handed leptons gives the following contribution:

$$\mathcal{L}_{\text{ferm}}^{\text{L-quarks}} = \overline{L}_i i (\partial_\mu - ig \frac{\vec{\sigma}}{2} \vec{W}_\mu) \gamma^\mu L_i$$
$$= \overline{(\nu \ l)}_{Li} i (\partial_\mu - ig \frac{\vec{\sigma}}{2} \vec{W}_\mu) \gamma^\mu \begin{pmatrix} \nu \\ l \end{pmatrix}_{Li}$$
$$= \frac{g}{\sqrt{2}} \overline{\nu_{Li}} \gamma_\mu W^{-\mu} l_{Li} + \frac{g}{\sqrt{2}} \overline{l_{Li}} \gamma_\mu W^{+\mu} \nu_{Li} + \cdots \quad (64)$$
$$= \frac{g}{\sqrt{2}} \overline{\nu_{Lk}^{\text{mass}}} (U_L^\nu U_L^{l\dagger})_{kj} \gamma_\mu W^{-\mu} l_{Lj}^{\text{mass}} + \frac{g}{\sqrt{2}} \overline{l_{Lk}^{\text{mass}}} (U_L^l U_L^{\nu\dagger})_{kj} \gamma_\mu W^{+\mu} \nu_{Lj}^{\text{mass}} + \cdots$$

The combination $(U_L^l U_L^{\nu\dagger})_{kj} = (U_L^\nu U_L^{l\dagger})_{kj}^\dagger$ is the Pontecorvo–Maki–Nakagawa–Sakata (PMNS) mixing matrix:

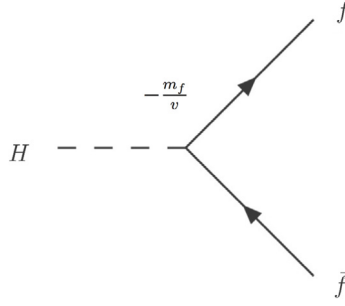$$U_{\text{PMNS}} = U_L^l U_L^{\nu\dagger}. \quad (65)$$

Fig. 2. Feynman diagram describing $H \rightarrow f\bar{f}$ at lowest order.

The interaction eigenstates and the mass eigenstates are equal for the charged leptons and rotated for the neutrinos:

$$\begin{pmatrix} e \\ \mu \\ \tau \end{pmatrix} = \begin{pmatrix} e^{\text{mass}} \\ \mu^{\text{mass}} \\ \tau^{\text{mass}} \end{pmatrix} \qquad \begin{pmatrix} \nu_e \\ \nu_\mu \\ \nu\tau \end{pmatrix} = \begin{pmatrix} U_{e1} & U_{e2} & U_{e3} \\ U_{\mu 1} & U_{\mu 2} & U_{\mu 3} \\ U_{\tau 1} & U_{\tau 2} & U_{\tau 3} \end{pmatrix} \begin{pmatrix} \nu_1 \\ \nu_2 \\ \nu_3 \end{pmatrix} \tag{66}$$

The equivalence of the mass and interaction eigenstates for the charged leptons is not a convention like for the up quarks but the experimental result of no flavor transition inside coherent beams. Neutrinos are chargeless fermions, the possibility for particle and anti-particle to be identical ($\nu_L = \overline{\nu_R}$) must be considered. The Lagrangian can contain only Dirac neutrinos, only Majorana neutrinos or both. The new mass term for the Majorana neutrinos is: $-m\overline{\nu}\nu$.

2.11. Higgs boson decays

For a specific process the expected cross section or the decay partial width can be calculated from the Lagrangian. Predictions for collider experiments may require the computation of tens of thousands of Feynman diagrams. This task is more suited to computers than to manual calculation. There are several computer programs available that calculate Feynman diagrams automatically, and making the predictions that will be compared with the results of experiments. Generators like ALPGEN [26], MadGraph [27], MC@NLO [28], POWHEG [29], Sherpa [30] and Whizard [31] perform a matching of matrix-element calculations and parton showers at LO or NLO in QCD. Multipurpose generators like PYTHIA [32] and Herwig [33] can simulate the Parton Shower (a model for multiple parton radiation), the Underlying Event (the residual part of the event in addition to the interesting process) and the Pile-Up (the multiple interaction in the same bunch crossing). However, only a limited set of the possible physics models beyond the Standard Model is implemented in these tools and implementing a new model into one of these codes needs practice. The package FeynRules [34] based on Mathematica tool [35] takes a model file with the Lagrangian as input and derives the Feynman rules [36] associated with it. The partial width of Higgs boson decay in two fermions (Fig. 2) can be calculated with a limited effort using the Feynman rules.

The vertex of the $H \rightarrow f\bar{f}$ diagram is: $g_{Hff} = -\frac{m_f}{v}$.

The matrix of the interaction derived from the Feynman rules:

$$\mathcal{M}_{\sigma_1,\sigma_2} = \overline{u}(p_1, \sigma_1) \left(-\frac{m_f}{v} \right) v(p_2, \sigma_2) \tag{67}$$

The squared transition amplitude is the sum of spinors of the squared matrix:

$$|\mathcal{M}|^2 = \sum_{\sigma_1,\sigma_2} |\mathcal{M}_{\sigma_1,\sigma_2} \mathcal{M}_{\sigma_1,\sigma_2}^\dagger| = \left(\frac{m_f}{v} \right)^2 \sum_{\sigma_1,\sigma_2} \overline{v}(p_2, \sigma_2) u(p_1, \sigma_1) \overline{u}(p_1, \sigma_1) v(p_2, \sigma_2) \tag{68}$$

Since there are no polarizations for the scalar Higgs boson the sum of spinors can be split:

$$\begin{aligned} |\mathcal{M}|^2 &= \left(\frac{m_f}{v} \right)^2 \sum_{\sigma_1} u(p_1, \sigma_1) \overline{u}(p_1, \sigma_1) \sum_{\sigma_2} \overline{v}(p_2, \sigma_2) v(p_2, \sigma_2) \\ &= \left(\frac{m_f}{v} \right)^2 \text{Tr}(\not{p}_1 + m_f) \text{Tr}(\not{p}_2 - m_f) \\ &= \left(\frac{m_f}{v} \right)^2 (4 p_1 p_2 - 4 m_f^2) \\ &= \left(\frac{m_f}{v} \right)^2 [2 M_H^2 - 8 m_f^2] \\ &= \left(\frac{m_f}{v} \right)^2 2 M_H^2 \beta^2 \end{aligned} \tag{69}$$
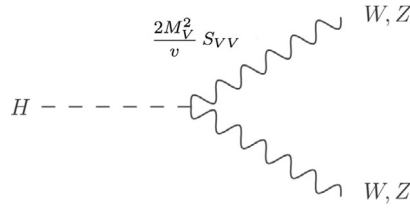
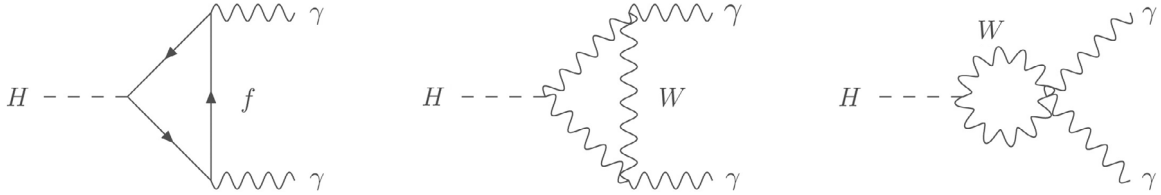**Fig. 3.** Feynman diagram describing $H \to VV$ at lowest order.

Fig. 4. Feynman diagrams describing the main $H \to \gamma\gamma$ contributions.

For the last step in Eq. (69) the following relations have been used: $p_1 + p_2 = s = M_H^2$ and $\beta = |p_f|/E_f = \sqrt{1 - \frac{4m_f^2}{m_H^2}}$. The color factor N_C must be added in case the fermions are quarks. The decay rate is related to the transition amplitude and to the phase space. The generic two-body decay rate, in the rest frame of a particle with mass M_H is:

$$\frac{d\Gamma}{d\Omega} = \frac{1}{32\pi^2}|\mathcal{M}|^2\frac{|p_f|}{M_H^2} \tag{70}$$

Including the transition amplitude, considering $|p_f| = \beta E_f = \beta M_H/2$ and doing the angular integration $\int d\Omega = 4\pi$ we find:

$$\Gamma(H \to f\bar{f}) = \frac{N_C}{8\pi v^2}m_f^2 M_H \beta^3 \tag{71}$$

For $m_f \ll M_H$, $\beta \sim 1$ and the decay rate results to be proportional to the squared mass of fermions and to the Higgs boson mass.

The vertex of the Feynman diagram for the Higgs boson coupling with the vector bosons W and Z (Fig. 3) comes from Eq. (46):

$$g_{HVV} = \frac{2M_V^2}{v}S_{VV} \tag{72}$$

The decay rate calculation for the $H \to VV$ diagram gives the following result:

$$\Gamma(H \to VV) = \frac{1}{16\pi v^2}M_H^3 S_{VV}(1 - x + \frac{3}{4}x^2)\sqrt{1-x} \tag{73}$$

where $x = \frac{4M_V^2}{M_H^2}$. Since the coupling of the Higgs boson to gauge bosons is large, the decay to VV can occur also if $M_H < 2M_V$ through the off-shell diagram $H \to V^*V$ where $M_{V^*} + M_V < 2M_V$ with rates even larger than fermions. The off-shell rate needs a dedicated calculation.

The Higgs boson does not couple directly with photons but it can decay to $\gamma\gamma$ through higher order diagrams, the main contributions are the top and W loops (Fig. 4). The total SM Higgs boson decay width as a function of M_H is shown in Fig. 5. The change of slope between 100 and 200 GeV is due to the V^*V and VV channels turn-on. For $M_H = 125$ GeV the expected total width is 4.09 MeV with $\pm0.7\%$ theoretical uncertainty [37]. While for the high mass Higgs boson the width can be measured directly, for the low mass Higgs boson this measurement is a challenge because the expected width ($\mathcal{O}(10)$ MeV) is dominated by the experimental resolution ($\mathcal{O}(10)$ GeV). The branching ratio BR($H \to X$) = $\Gamma_{H\to X}/\Gamma_H$, which is the probability for the Higgs boson to decay into the final state X is given in Fig. 6 (left) for a wide M_H range and in Fig. 6 (right) for M_H around 125 GeV. The uncertainties on the Higgs boson branching ratios for Higgs boson masses around 125 GeV are about 0.5% for the $H \to \tau^+\tau^-$, $H \to \mu^+\mu^-$, $H \to W^+W^-$ and $H \to ZZ$ decays and are dominated by the theoretical uncertainties, for the $H \to b\bar{b}$ and $H \to c\bar{c}$ decays the uncertainties are respectively 2% and 5% and are dominated by the quark mass parameters. The branching ratio of the $b\bar{b}$ decay channel at $M_H \sim 125$ GeV is about two orders of magnitude larger than the $\gamma\gamma$ channel but at hadron colliders the latter can be reconstructed with higher signal significance. The reason is the large background
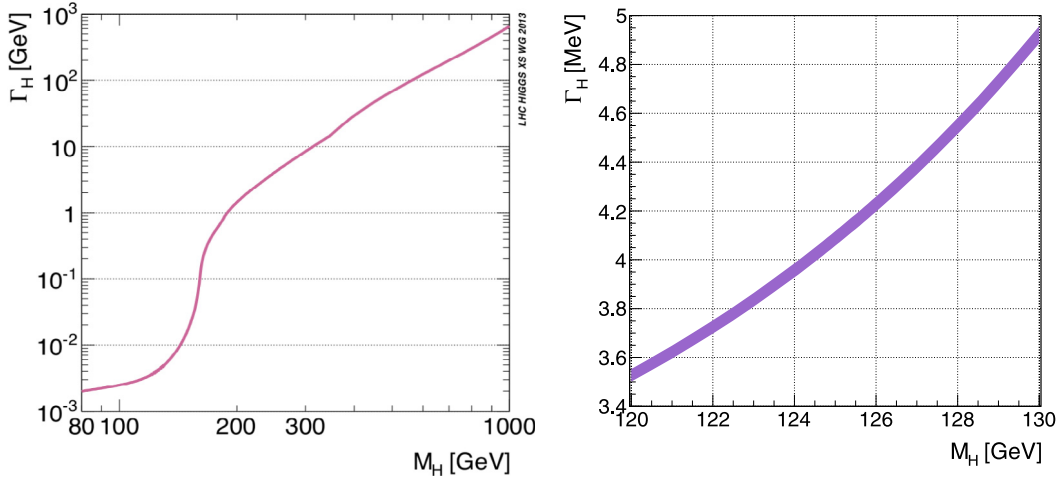
Fig. 5. The *SM* Higgs boson total decay width and its uncertainty in a wide mass range (left) from Ref. [38] and around 125 GeV (right) from Ref. [37].
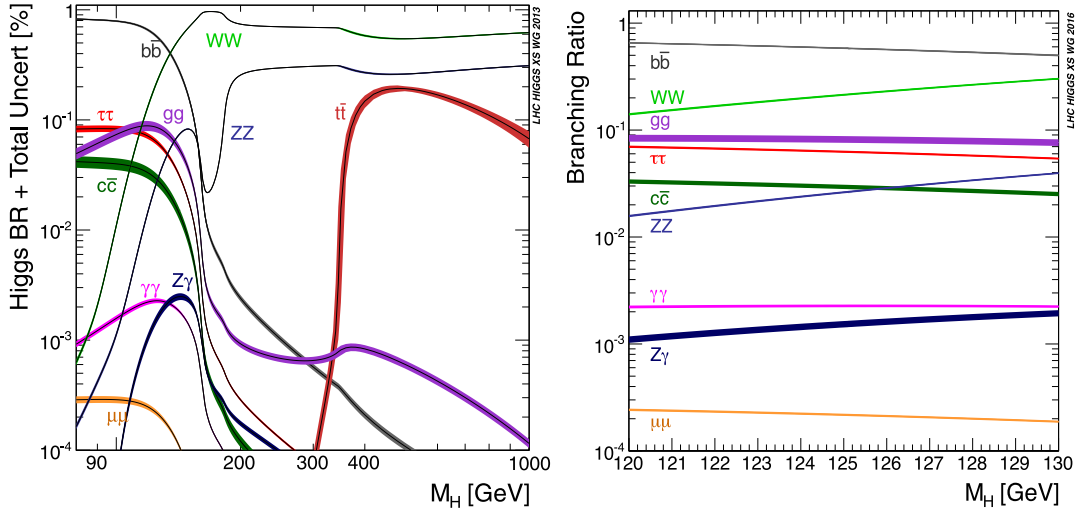

Fig. 6. The *SM* Higgs boson branching ratios and their uncertainties for the full mass range (left) from Ref. [38] and around 125 GeV (right) from Ref. [37].

of the $b\bar{b}$ channel and the difficult separation between signal and background. More details concerning the *SM* Higgs boson decays and the Higgs boson properties can be in found in Ref. [37] and [38].

3. Higgs boson searches at electron–positron colliders

3.1. Higgs boson production at e^+e^- colliders

The direct coupling of the Higgs boson with a light fermion like the electron is negligible but other production mechanisms are possible. The evolution of the leading order $e^+e^- \rightarrow HX$ production cross sections with center-of-mass energy is shown in Fig. 7 for a Higgs boson mass of $M_H = 126$ GeV. At electron–positron colliders the Higgs–strahlung (Fig. 8a) is the dominant production process if $\sqrt{s}$ is close to the threshold $M_H + M_Z \simeq 220$ GeV. As the center of mass energy increases the Higgs–strahlung cross-section falls off as $1/s$, the *W*-boson fusion and *Z*-boson fusions (Fig. 8b) becomes the larger contribution respectively at $\sqrt{s} > 450$ GeV and $\sqrt{s} > 900$ GeV. The Higgs boson can be produced in association with top pairs over the threshold $M_H + 2m_t \simeq 470$ GeV (Fig. 9a). Double Higgs boson with Higgs boson self-coupling can be produced via Higgs–strahlung over the threshold of $2M_H + M_Z \simeq 340$ GeV (Fig. 9b) and via vector-boson fusion over the threshold $2M_H + 2M_W \simeq 410$ GeV (Fig. 9c).
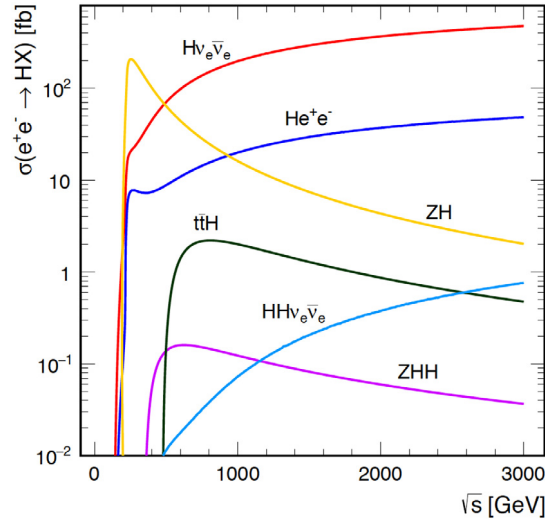
Fig. 7. Cross section as a function of center-of-mass energy for the main Higgs boson production processes at an e^+e^- collider for a Higgs boson mass of $M_H = 126$ GeV [39]. The values shown correspond to unpolarized beams and do not include the effect of bremsstrahlung.
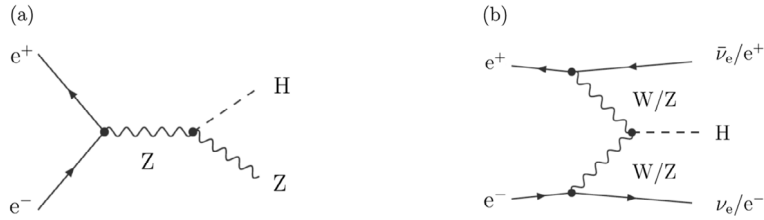

Fig. 8. Feynman diagrams for the Higgs boson production via Higgs–strahlung (a) and vector-boson fusion (b).
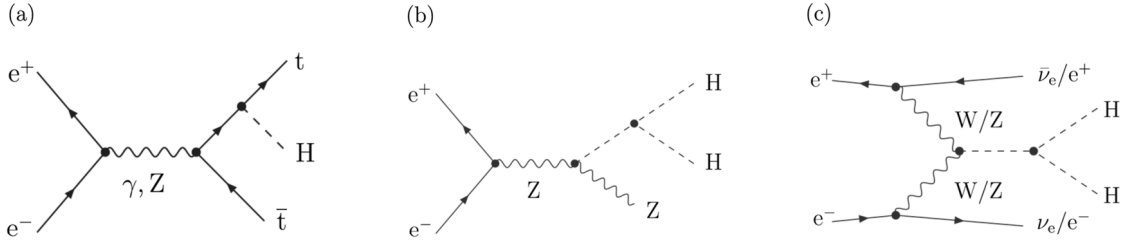

Fig. 9. Feynman diagrams for the Higgs boson production associated with top pairs (a) and double Higgs boson with Higgs boson self-coupling produced via Higgs–strahlung (b) and via vector-boson fusion (c).

3.2. Higgs boson searches at LEP

The phenomenological confirmation of the Higgs mechanism requires finding the Higgs boson, measuring the mass, the quantum numbers and verifying the proportionality of the Higgs coupling constants with the mass of the coupled particles. A significant mass range in the Higgs boson search was possible only from 1989 with the start of the Large Electron Positron Collider (LEP). LEP II reached the maximum center-of-mass energy of 209 GeV and ended the activity with the last beam dump on November 2nd 2000. With the maximum energy reached at the LEP collider the search for the Higgs boson signal was possible for masses up to 110–120 GeV (Fig. 10). Searches at LEP were performed in the following four channels:

- "four-jets" $ZH \rightarrow q\bar{q}b\bar{b}$,
- "missing-energy" $ZH \rightarrow \nu\bar{\nu}b\bar{b}$,
- "tau" $ZH \rightarrow q\bar{q}\tau^+\tau^-$ and $ZH \rightarrow \tau^+\tau^-b\bar{b}$,
- "electron and muon" $ZH \rightarrow e^+e^-b\bar{b}$ and $ZH \rightarrow \mu^+\mu^-b\bar{b}$.
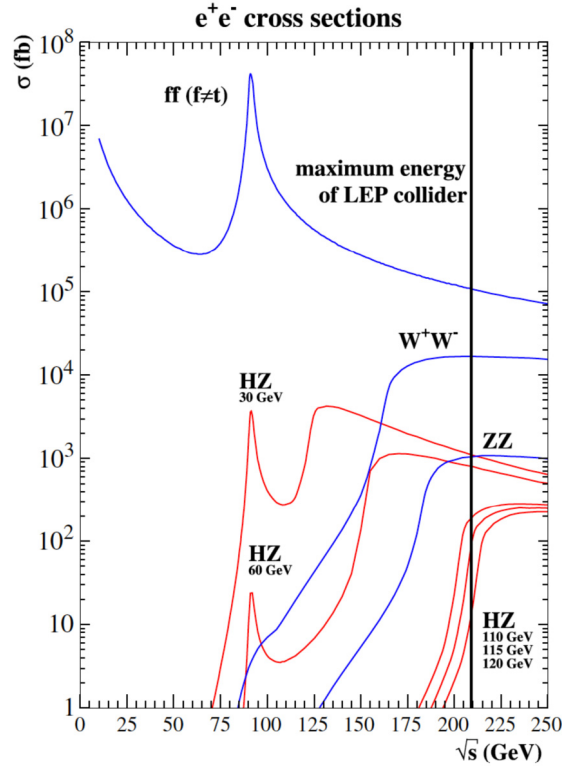
Fig. 10. Cross sections for Z boson, di-bosons and Higgs boson production as a function of the center-of-mass energy for Higgs boson masses of 30, 60, 110, 115, 120 GeV produced with PYTHIA [32].
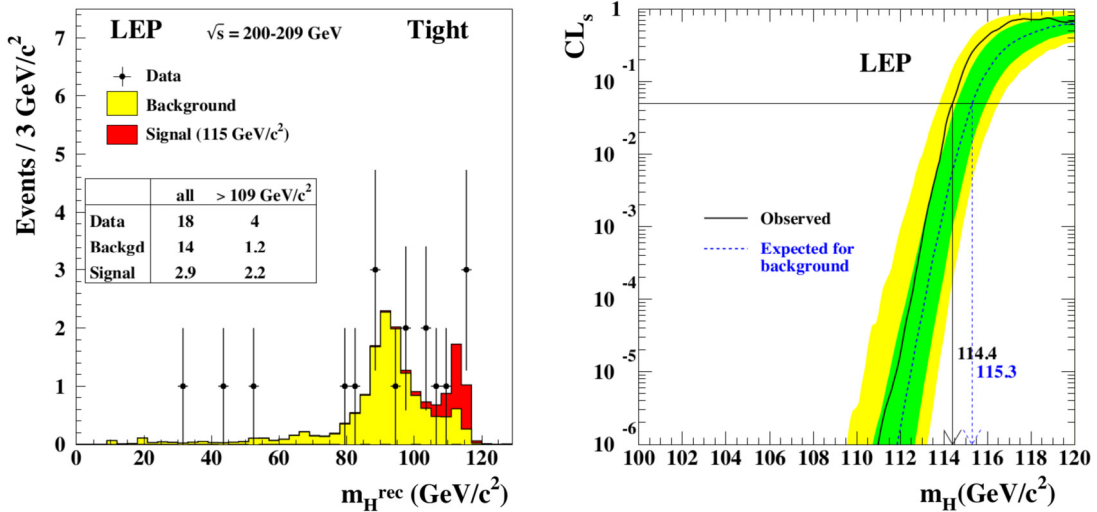
Fig. 11. Final results of the Higgs boson searches at LEP obtained by combining the four experiments [40]: mass distribution of tightly selected Higgs boson candidates compared to signal and background expectations (left), the confidence level $CL_s = CL_{s+b}/CL_b$ for the signal plus background hypothesis, as a function of the test mass m_H (right).

The fraction of the total decay rate for those final states depends on the Higgs boson branching ratio which in turn depends on the Higgs boson mass, this fraction is 77% for $M_H = 115$ GeV and larger for lower masses. The final mass distribution obtained from the combination of the four LEP experiments after tight selection requirements is shown in Fig. 11 (left). The frequentist exclusion limit is usually computed from the confidence CL_{s+b} for the signal plus background hypothesis but large downward fluctuation of the background could allow hypothesis to be excluded for which the experiment has no

Table 1
Expected and observed limits on the Standard Model Higgs boson mass at 95% confidence level for all LEP data combined and for the individual experiments [40].

	exp. limit	obs. limit
LEP	115.3 GeV	114.4 GeV
ALEPH	113.5 GeV	111.5 GeV
DELPHI	113.3 GeV	114.3 GeV
L3	112.4 GeV	112.0 GeV
OPAL	112.7 GeV	112.8 GeV

sensitivity due to the small expected signal rate. To avoid this problem a more conservative limit was estimated with the ratio $CL_s = CL_{s+b}/CL_b$. The lowest test mass giving $CL_s = 0.05$ compatibility in Fig. 11 (right) was taken as the lower bound on the mass exclusion at the 95% confidence level:

LEP II combination [40] : $M_H > 114.4$ GeV at 95% CL_s

The limits for each individual experiments (Table 1) are not very different from the LEP combination. The presence of a signal can be inferred from the confidence 1 - CL_b (also called local p-value) expressing the level of consistency with the background hypothesis. With a gaussian approximation $p_b = 2.7 \times 10^{-3}$ ($p_b = 5.7 \times 10^{-7}$) would indicate a 3σ (5σ) excess beyond the background expectation. The slight excess at $M_H = 115$ GeV, dominated by the "four-jet" channel of the ALEPH experiment, has a p-value of 0.09.

3.3. Higgs boson searches at future e^+e^- colliders

The LEP limit will probably not be the end of the history for the Higgs boson physics at electron–positron colliders. New colliders are under consideration by the physics community:

- the FCC-ee;
- the Circular Electron Positron Collider (CEPC) [41] with $\sqrt{s} = 240$ GeV;
- the International Linear Collider (ILC) [42] with $\sqrt{s}$ up to 1 TeV;
- the Compact Linear Collider (CLIC) [39] with $\sqrt{s}$ up to 3 TeV.

The main goal of these new accelerators are:

(a) measurement of the properties of the Higgs boson with very high precision;
(b) measurement of the properties of the top quark with very high precision;
(c) searches of new particles expected in models of physics at the TeV energy scale.

The schedule planning for ILC and CEPC is to start data taking by the end of next decade, for CLIC and FCC-ee is to start by the middle of 2030's after the end of the LHC physics program.

In e^+e^- collisions, considering the precise knowledge of the center-of-mass four-momentum $p_{c.m.}$ ($\sqrt{s}, 0, 0, 0$) in the laboratory frame, the $e^+e^- \to HZ$ production process provides a precise measurement of the Higgs boson mass with the recoil mass method. Given the mass and the energy of the reconstructed Z boson, the Higgs boson mass can be extrapolated from the conservation of the four-momentum:

$$p_H^2 = (p_{c.m.} - p_Z)^2 \qquad m_H^2 = s + m_Z^2 - 2p_{c.m.}p_Z \tag{74}$$

$$m_H = m_{recoil} = \sqrt{s + m_Z^2 - 2\sqrt{s}E_Z} \tag{75}$$

The expected recoil mass distribution at the ILC collider for a $m_H = 125$ GeV Higgs boson with 250 fb^{-1} at $\sqrt{s} = 250$ GeV and for the $Z \to \mu^+\mu^-$ decay is shown in Fig. 12. The Higgs boson mass can be measured with a resolution better than 30 MeV [43].

The studies presented for the different e^+e^- future colliders are based on scenarios with different energy stages. For the CLIC collider three energy stages have been considered: $\sqrt{s} = 350$ GeV, $\sqrt{s} = 1.4$ TeV and $\sqrt{s} = 3$ TeV. The lower energy is motivated by the measurement of the HZ coupling. The cross section of the Higgs–strahlung is higher at 250 GeV but with a single stage at 350 GeV it will be possible to study the three processes HZ, $H\nu_e\bar{\nu}_e$ and $t\bar{t}$. The stage at $\sqrt{s} = 1.4$ TeV will allow a precise measurement of the $H\nu_e\bar{\nu}_e$ and He^+e^- processes. The five measurements described in Table 2 can provide the measurement of the four parameters g_{HZZ}, g_{HWW}, g_{Hbb} and Γ_H. The coupling parameters are the same couplings used in Section 2.11. The Standard Model expected value $\Gamma_H \sim 4$ MeV is too small to be measured directly from the shape of the Higgs boson resonance but Γ_H can be estimated from the fit of these observables. Considering a wider list of 26
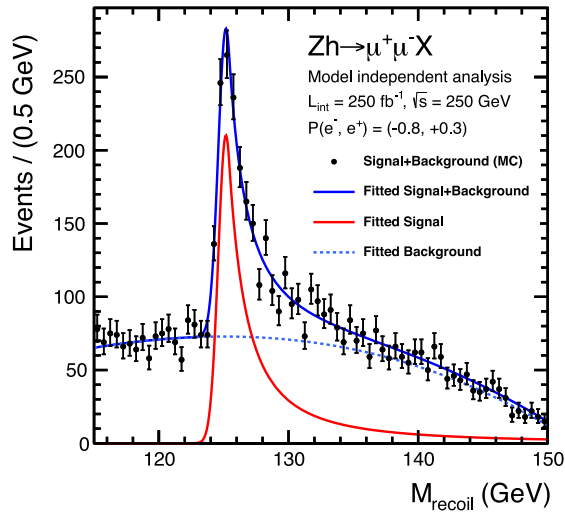
Fig. 12. Recoil mass distribution expected at the ILC collider for the process: $e^+e^- \to Zh$ followed by $Z \to \mu^+\mu^-$ decay for $m_H = 125$ GeV with 250 fb^{-1} at $\sqrt{s} = 250$ GeV [43].

Table 2
Example of five measurements for Higgs boson production via Higgs–strahlung (ZH) and vector boson fusion ($H\nu_e\bar{\nu}_e$, He^+e^-) and the associated observables related to the parameters g_{HZZ}, g_{HWW}, g_{Hbb} and Γ_H.

Channel	Measurement	Observable
ZH	$\sigma(ZH) \times BR(H \to b\bar{b})$	$g_{HZZ}^2 g_{Hbb}^2 / \Gamma_H$
$H\nu_e\bar{\nu}_e$	$\sigma(H\nu_e\bar{\nu}_e) \times BR(H \to b\bar{b})$	$g_{HWW}^2 g_{Hbb}^2 / \Gamma_H$
$H\nu_e\bar{\nu}_e$	$\sigma(H\nu_e\bar{\nu}_e) \times BR(H \to WW^*)$	g_{HWW}^4 / Γ_H
$H\nu_e\bar{\nu}_e$	$\sigma(H\nu_e\bar{\nu}_e) \times BR(H \to ZZ^*)$	$g_{HWW}^2 g_{HZZ}^2 / \Gamma_H$
He^+e^-	$\sigma(He^+e^-) \times BR(H \to b\bar{b})$	$g_{HZZ}^2 g_{Hbb}^2 / \Gamma_H$

Table 3
Expected relative precision for Higgs boson couplings and Γ_H at the CLIC collider for different energies and integrated luminosities with a model-independent fit [39]. Values marked "–" cannot be measured with sufficient precision at the given energy. The three couplings with massless particles $g_{Hgg}^\dagger$, $g_{H\gamma\gamma}^\dagger$ and $g_{HZ\gamma}^\dagger$ are "effective". Operation with -80% longitudinal electron spin-polarization is assumed above 1 TeV.

Parameter	Relative precision		
	350 GeV 500 fb^{-1}	+1.4 TeV +1.5 ab^{-1}	+3 TeV +2 ab^{-1}
g_{HZZ}	0.8%	0.8%	0.8%
g_{HWW}	1.4%	0.9%	0.9%
g_{Hbb}	3.0%	1.0%	0.9%
g_{Hcc}	6.2%	2.3%	1.9%
$g_{H\tau\tau}$	4.3%	1.7%	1.4%
$g_{H\mu\mu}$	–	14.1%	7.8%
g_{Htt}	–	4.2%	4.2%
$g_{Hgg}^\dagger$	3.7%	1.8%	1.4%
$g_{H\gamma\gamma}^\dagger$	–	5.7%	3.2%
$g_{HZ\gamma}^\dagger$	–	15.6%	9.1%
Γ_H	6.7%	3.7%	3.5%

measurements, the expected precision for their 11 related parameters is described in Table 3 [39]. The fit is performed in three stages, taking the statistical uncertainties obtainable at the previous energy stage into account. With a model-independent fit, many of the couplings can be measured with a precision better than 2% and the total Higgs boson width can
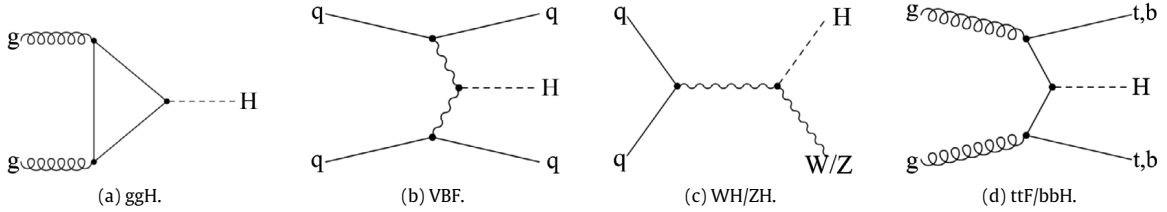
Fig. 13. Leading-order Feynman diagrams for the main *SM* Higgs boson production channels at hadron colliders: (a) gluon fusion, (b) vector-boson fusion, (c) associated production with one vector boson, (d) heavy-quark associated production.
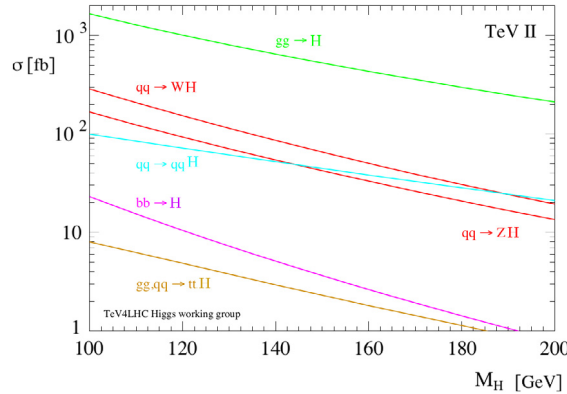

Fig. 14. The Standard Model Higgs boson production cross sections for Tevatron at $\sqrt{s} = 1.96$ TeV, as predicted by the TeV4LHC study group [44]. Results for $gg \to H$, $q\bar{q} \to VH$, $b\bar{b} \to H$ are at NNLO in the QCD expansion. Vector boson fusion and $t\bar{t}$ associated production are at NLO accuracy.

be measured with a precision of 3.5%. With a model-dependent fit where the Higgs boson can decay only in the *SM* channels the total Higgs boson width can be measured with a precision of 1.1%.

4. Higgs boson searches and measurements at hadron colliders

4.1. Higgs boson production at hadron colliders

The Higgs boson production at the LHC mainly occurs through the following processes, listed in order of decreasing cross section:

- gluon fusion production $gg \to H$ (Fig. 13a);
- vector boson fusion production $qq \to qqH$ (Fig. 13b);
- associated production with one vector boson (Fig. 13c);
- associated production with a pair of heavy quarks (Fig. 13d).

The cross sections of various Higgs boson production channels depends on the type of colliding hadrons, on the collision energy and on the Higgs boson mass. The cross sections for the Tevatron $p\bar{p}$ collider at its center-of-mass energy of $\sqrt{s} = 1.96$ TeV are shown in Fig. 14 as a function of the Higgs boson mass. The cross sections for the LHC pp collider are shown in Fig. 15 (left) at the energy $\sqrt{s} = 13$ TeV as a function of the Higgs boson mass and in Fig. 15 (right) for $M_H = 125$ GeV as a function of the center-of-mass-energy. The dominant Higgs boson production process is the gluon–gluon fusion for both colliders. The gluon–gluon fusion is strongly dominated by top-quark loops (Fig. 13a). At Tevatron the *WH/ZH* Higgs–strahlung production channels compete with the VBF channel since the Higgs–strahlung proceed via $q\bar{q}$ interaction and q, $\bar{q}$ are both valence quarks in $p\bar{p}$ collisions. For the same reason $t\bar{t}H$ production is largely dominated by $q\bar{q}$ annihilation at Tevatron and by gluon fusion at the LHC. The increase of the LHC energy leads to more abundant Higgs boson production. The total *SM* Higgs boson cross section at the LHC estimated at N³LO QCD order is 19 pb at 7 TeV and 62 pb at 14 TeV [37]. The uncertainties are about 5% with 4% of contribution due to the scale factor, 3% due to the strong coupling constant α_s and 2% due to parton distribution functions. Increasing the LHC energy by a factor 2, the total Higgs boson cross sections can be increased by a factor 3.3. On the other hand also the Standard Model backgrounds significantly increase their cross sections at higher energies. The *ZZ* cross section estimated at NNLO QCD order is 6.7 pb at 7 TeV and 19 pb at 14 TeV (Fig. 16 left) with an increase factor of 2.8. The W⁺W⁻ cross section estimated at NNLO QCD order is 49 pb at 7 TeV and 131 pb at 14 TeV
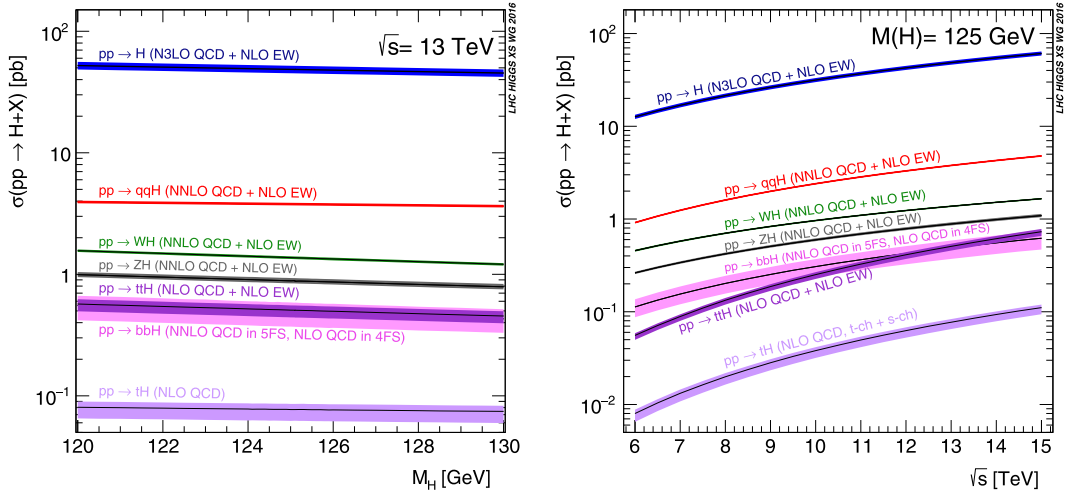
Fig. 15. The Standard Model Higgs boson production cross sections for LHC pp collisions at $\sqrt{s} = 13$ TeV as a function of Higgs boson mass (left) and Higgs boson production cross sections as a function of the center-of-mass-energies for $M_H = 125$ GeV (right) [37]. The size of the bands reflects the estimated theoretical uncertainties. The total cross section uncertainty is about 5%.
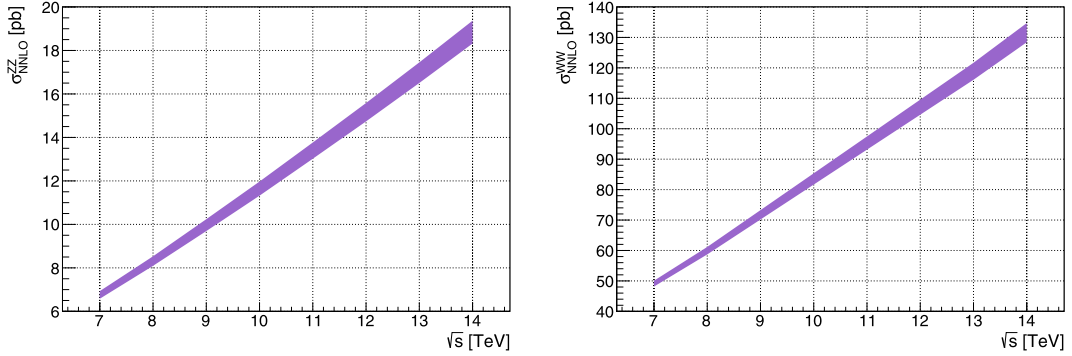

Fig. 16. Inclusive cross sections at the LHC for ZZ production at NNLO QCD order [45] (left), for W^+W^- production at NNLO QCD order [46] (right). The size of the bands of about 3% reflects the estimated theoretical uncertainties.

(Fig. 16 right) with an increase factor of 2.7. The σ^{ZZ} and σ^{WW} uncertainties are about 3%. The reasons to increase the LHC energy up to the accelerator limit are to increase the Higgs boson production cross section and to increase the probability of new physics discovery.

4.2. Higgs boson signal strength and coupling modifiers

The signal strength, defined as the ratio of the measured Higgs boson rate to its *SM* prediction, is used to characterize the Higgs boson yields. This ratio depends on the production cross section and on the branching ratio. Different ratios μ_i^f can be considered depending on the production process "i" and on the decay channel "f"

$$\mu_i^f = \frac{\sigma_i}{(\sigma_i)_{SM}} \frac{BR^f}{(BR^f)_{SM}} = \frac{\sigma_i}{(\sigma_i)_{SM}} \frac{\Gamma^f/\Gamma_H}{(\Gamma^f/\Gamma_H)_{SM}} \tag{76}$$

The coupling modifiers are introduced for every production process or decay mode:

$$k_i^2 = \frac{g_{Hii}}{(g_{Hii})_{SM}} = \frac{\sigma_i}{(\sigma_i)_{SM}} \qquad k_f^2 = \frac{g_{Hff}}{(g_{Hff})_{SM}} = \frac{\Gamma^f}{(\Gamma^f)_{SM}} \tag{77}$$

If $\Gamma_H = (\Gamma_H)_{SM}$, the signal strength is simply the product of the production and the decay coupling modifiers:

$$\mu_i^f = k_i^2 k_f^2 . \tag{78}$$

Tables 4 and 5 describe the coupling modifiers for the different Higgs boson production processes and decay channels. Individual coupling modifiers correspond tree-level Higgs boson couplings to different particles. For σ(VBF) the two

Table 4
Coupling modifiers for the main *SM* Higgs boson production processes at hadron colliders.

Production	Coupling modifier
$\sigma(\text{ggH})$	$1.06\,k_t^2 + 0.01\,k_b^2 + 0.01\,k_t k_b$
$\sigma(\text{VBF})$	$0.74\,k_W^2 + 0.26\,k_Z^2$
$\sigma(\text{WH})$	k_W^2
$\sigma(\text{ttH})$	k_t^2
$\sigma(\text{bbH})$	k_b^2

Table 5
Coupling modifiers for the main *SM* Higgs boson decays.

Decay	Coupling modifier
Γ^{ZZ}	k_Z^2
Γ^{WW}	k_W^2
$\Gamma^{\gamma\gamma}$	$1.059\,k_W^2 + 0.07\,k_t^2 - 0.66\,k_t k_W$
$\Gamma^{\tau\tau}$	k_τ^2
Γ^{bb}	k_b^2

contributions are due to the Z and W bosons, for $\sigma(ggH)$ the three contributions are due to the top quark and bottom quark loops and their interference, for $\Gamma^{\gamma\gamma}$ the three contributions are due to the W and top quark loops and their interference.

4.3. Higgs boson searches at Tevatron

The Tevatron Run II provided proton–antiproton collisions at the center-of-mass energy of 1.96 TeV from 2001 until autumn 2011. The two experiments CDF and D0 each collected 10 fb^{-1} of integrated luminosity. In proton colliders the total inelastic cross section due to processes mediated by the strong force is more than ten orders of magnitude higher than the cross section for Higgs boson production. The main problem is therefore the signal extraction starting from the trigger up to the offline selection. In the last Tevatron combination [47] the Higgs boson was searched in the mass range between 90 and 200 GeV/c^2. The considered Higgs boson production processes were the vector boson fusion (Fig. 13b), the associated production with a vector boson (Fig. 13c), and the associated production with top quarks through gluon–gluon fusion (Fig. 13d). The considered Higgs boson decays were $H \rightarrow b\bar{b}$, $H \rightarrow W^+W^-$, $H \rightarrow ZZ$, $H \rightarrow \tau^+\tau^-$, and $H \rightarrow \gamma\gamma$. Below 130 GeV/c^2 the $WH \rightarrow l\nu b\bar{b}$ and $ZH \rightarrow l^+l^-b\bar{b}$ searches give the most contribution to the search sensitivity, above 130 GeV/c^2 the $H \rightarrow W^+W^-$ channel contributes majority of the sensitivity. The observed and the expected 95% C.L. Bayesian exclusion limits for the Higgs boson cross section ratio σ/σ_{SM} are shown in Fig. 17 as a function of the test mass m_H. In the mass ranges where $\sigma/\sigma_{SM} < 1$ the *SM* Higgs boson is excluded at 95% C.L. or more. The not excluded regions at 95% C.L. Bayesian are:

$$M_H < 90\,\text{GeV} \qquad 109\,\text{GeV} < M_H < 149\,\text{GeV} \qquad M_H > 182\,\text{GeV}$$

The observed and expected cross sections have been compared using CL$_s$ and CL Bayesian statistical methods. The difference in terms of cross sections between the two methods is less than 5% for every Higgs boson mass, the resulting differences for the exclusion limits are negligible. An excess of events over 2 standard deviations is present in the mass range between 115 GeV and 140 GeV, the local significance at $m_H = 125$ GeV corresponds to 3 standard deviations. To characterize the compatibility of this excess with the signal-plus-background hypothesis, the best-fit of the signal strength $\mu = \sigma/\sigma_{SM}$ is computed using the Bayesian calculation. The best fit values of the signal strength are shown in Fig. 18 (left) as a function of the Higgs boson mass, at 125 GeV/c^2 the best fit of $\mu = \sigma/\sigma_{SM}$ is $1.44^{+0.49}_{-0.47}(\text{stat.})^{+0.33}_{-0.31}(\text{syst.}) \pm 0.10(\text{theory})$. The best fit values of the signal strength are shown in Fig. 18 (right) for the decays channels $H \rightarrow \gamma\gamma$, $H \rightarrow W^+W^-$, $H \rightarrow \tau^+\tau^-$ and $VH \rightarrow Vb\bar{b}$ for a Higgs boson mass of 125 GeV. All the measured signal strengths are compatible with 1.

4.4. Higgs boson searches at LHC with collision data at $\sqrt{s} = 7$ and 8 TeV

The full set of collision data collected at $\sqrt{s} = 7$ and 8 TeV between 2010 and 2012 is called Run 1. The Run 1 can be divided in three periods:

- the 2011 data samples led to new stringent mass limits;
- adding part of the 2012 data samples led to the Higgs boson discovery;
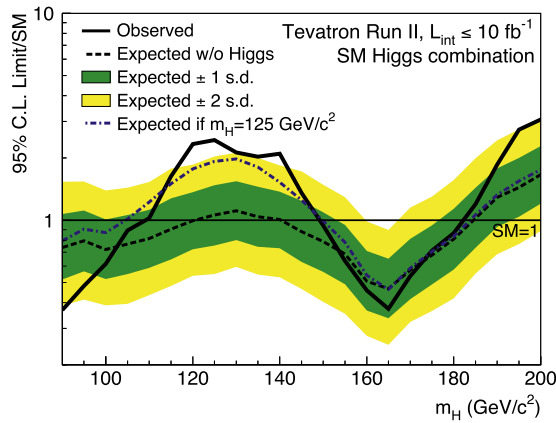- the full Run 1 allowed the study of Higgs boson properties.

Fig. 17. The observed and the expected 95% C.L. Bayesian exclusion limits expressed in terms of the cross section ratio σ/σ_{SM} as a function of Higgs boson mass for the combined CDF and D0 searches in all decay modes [47]. The expected limit is for the background-only hypothesis. The short-dashed line shows median expected limits assuming a *SM* Higgs boson is present with $m_H = 125\,\text{GeV}/c^2$.
Source: Reprinted figure with permission from [47].
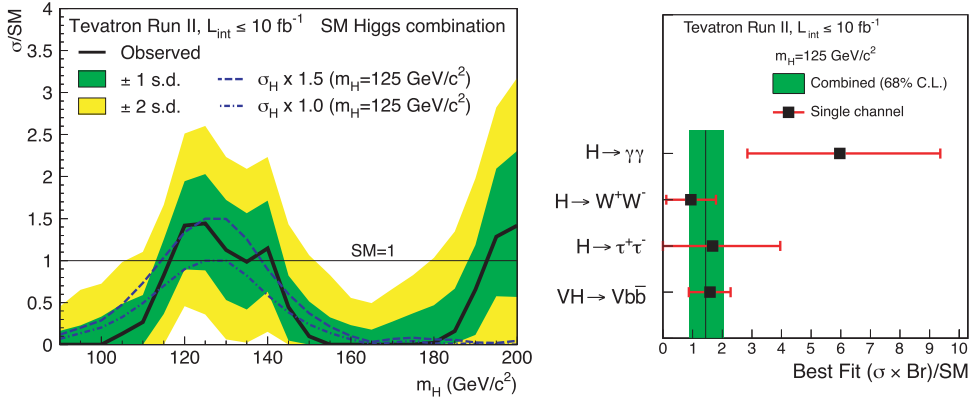ⓒ 2013, by the American Physical Society.

Fig. 18. The best-fit values of the signal strength as a function of Higgs boson mass for the combined CDF and D0 searches in all decay modes [47]. The dashed line gives the expected best-fit signal strengths including a *SM* Higgs boson with $m_H = 125\,\text{GeV}$. The short-dashed line gives the expected best-fit signal strengths when the cross section of the 125 GeV Higgs boson is increased by 50% (left). The best-fit values of the signal strength for the combined CDF and D0 searches focused for different decay channels for a Higgs boson mass of 125 GeV (right).
Source: Reprinted figure with permission from [47].
ⓒ 2013, by the American Physical Society.

Table 6
The most relevant events of the LHC Run 1.

Date	$\sqrt{s}$	Description
November 23rd 2009	900 GeV	First pilot collisions and trial ramp
December 6th 2009	900 GeV	Stable beams
December 16th 2009	2.36 TeV	First collisions in all four experiments
March 30th 2010	7 TeV	First colliding beams
April 5th 2012	8 TeV	First colliding beams
June 18th 2012	8 TeV	Technical stop after delivering 6 fb^{-1}
February 16th 2013	8 TeV	LHC long stop (LS1) for magnet repair

4.4.1. The results with collision data at $\sqrt{s} = 7$

In March 30th 2010, the first proton–proton collisions took place in the LHC at the center-of-mass energy of 7 TeV. This unprecedented energy record was reached with several commissioning steps as described in Table 6. The first year of data taking at 7 TeV, from March 30th 2010 to November 3rd 2010, can be considered a commissioning period. The maximum instantaneous luminosity was $\sim 3.6 \times 10^{32}\,\text{cm}^{-2}\,\text{s}^{-1}$ and the recorded integrated luminosities were 45 pb^{-1} for ATLAS and 43 pb^{-1} for CMS. The second year of data collection at 7 TeV, from March 14th 2011 to October 30rd 2011, the maximum instantaneous luminosity increased up to $\sim 3.5 \times 10^{33}\,\text{cm}^{-2}\,\text{s}^{-1}$ and the recorded integrated luminosities were 5.25 pb^{-1}
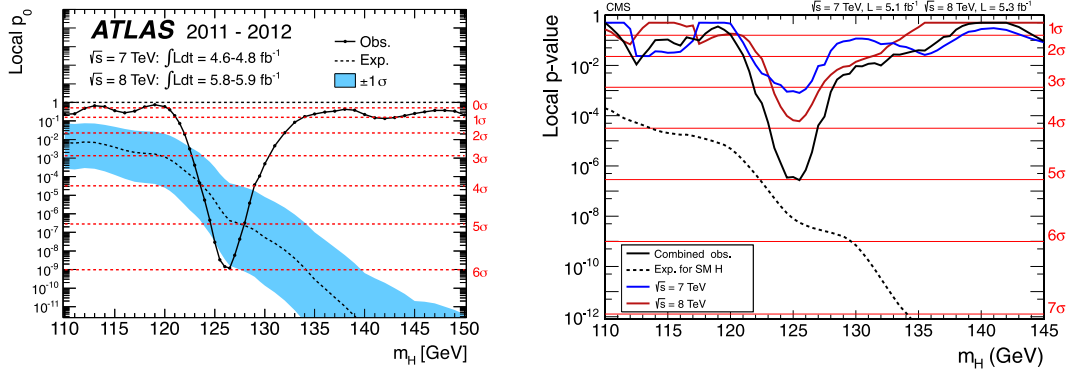
Fig. 19. The local p-values observed by the ATLAS experiment from the combination of the different Higgs boson decay channels and the combination of $\sqrt{s} = 7$ TeV and $\sqrt{s} = 8$ TeV as a function of the *SM* Higgs boson mass [50]. The dashed line shows the expected local p-values for a *SM* Higgs boson like with its $\pm\sigma$ band (left). The local p-values observed by the CMS experiment from the combination of the different Higgs boson decay channels for $\sqrt{s} = 7$ TeV and $\sqrt{s} = 8$ TeV and their combination as a function of the *SM* Higgs boson mass [51]. The dashed line shows the expected local p-values for a *SM* Higgs boson with a mass m_H (right).

for ATLAS and 5.20 fb^{-1} for CMS. Direct Higgs boson searches at LHC based on data corresponding to $\sim$5 pb^{-1} of integrated luminosity per experiment collected at $\sqrt{s} = 7$ TeV were able to set only exclusion limits. The CMS experiment excluded at 95% C.L. the range of masses from 127 to 600 GeV [48]. The ATLAS experiment excluded at 95% C.L. the ranges of masses 111.4–116.6, 119.4–122.1 and 129.2–541 GeV [49]. In the remaining not excluded regions:

- ATLAS observed an excess of events at 126 GeV with a local significance corresponding to 2.9 σ;
- CMS observed an excess of events at 124 GeV with a local significance corresponding to 3.1 σ.

4.4.2. The Higgs boson discovery

LHC started beam collisions at the energy of 8 TeV in April 5th 2012. The instantaneous luminosity reached a maximum of $\sim$7.7 × 10^{33} cm^{-2} s^{-1}. After only 2 months and half before a technical stop CMS and ATLAS recorded respectively 5.30 fb^{-1} and 5.80 fb^{-1} of integrated luminosities. In July 4th 2012 the ATLAS and CMS Collaborations reported at a seminar at CERN and at the ICHEP 2012 conference in Melbourne the observation of a new particle with a mass of approximately 125 GeV and Higgs-boson-like properties [50,51]. The data samples used in the analysis corresponded to the integrated luminosities of about 5 fb^{-1} collected at 7 TeV and 6 fb^{-1} collected at 8 TeV per experiment. The considered Higgs boson decays channels were $H \rightarrow b\bar{b}$, $H \rightarrow W^+W^-$, $H \rightarrow ZZ$, $H \rightarrow \tau^+\tau^-$, and $H \rightarrow \gamma\gamma$. ATLAS observed an excess of events with a best fit mass $m_H = 126.0 \pm 0.4(\text{stat.}) \pm 0.4(\text{syst.})$ GeV with a local significance of 6σ (Fig. 19 left). CMS observed an excess of events with a best fit mass $m_H = 125.3 \pm 0.4(\text{stat.}) \pm 0.5(\text{syst.})$ GeV with a local significance of 5σ (Fig. 19 right).

The signal strengths $\mu_i = \sigma_i/(\sigma_i)_{SM}$ were compatible to 1 for each decay channel for both experiments (Fig. 20). The measured signal strength combinations were $\mu = 1.4 \pm 0.3$ for ATLAS and $\mu = 0.87 \pm 0.23$ for CMS.

4.4.3. The Higgs boson characterization

At the end of the Run 1, in December 16th 2012, the recorded integrated luminosities at $\sqrt{s} = 8$ TeV have been quadruplicated for both experiments. To test the compatibility of the observed new resonance with the expected properties of the *SM* Higgs bosons it is important to measure, in addition to the mass and the signal strength, all the Higgs boson properties experimentally accessible at the LHC.

4.4.4. The Higgs boson mass measurement

The Higgs boson mass can be measured with the $H \rightarrow ZZ \rightarrow 4l$ and $H \rightarrow \gamma\gamma$ decay channels, their observed invariant mass distributions using the full Run 1 data sample are shown in Fig. 32. In order to quantify the compatibility of the data with the expected signal, a profile likelihood test statistics Λ is built that compares the background only with the signal plus background hypothesis:

$$\Lambda(m_H) = -2\ln\frac{\mathcal{L}(n \mid b, \hat{\theta}_0)}{\mathcal{L}(n \mid \hat{\mu} \cdot s(m_H) + b, \hat{\theta})} \tag{79}$$

where n is the number of observed events, $s(m_H)$ stands for the signal expected under the *SM* Higgs boson hypothesis, b stands for backgrounds and θ are nuisance parameters describing systematic uncertainties. The signal s is multiplied by the signal strength factor μ to perform a mass measurement reducing the dependence of the result on assumptions about the *SM* Higgs boson couplings and about the variation of the production cross section times branching fraction with the mass.
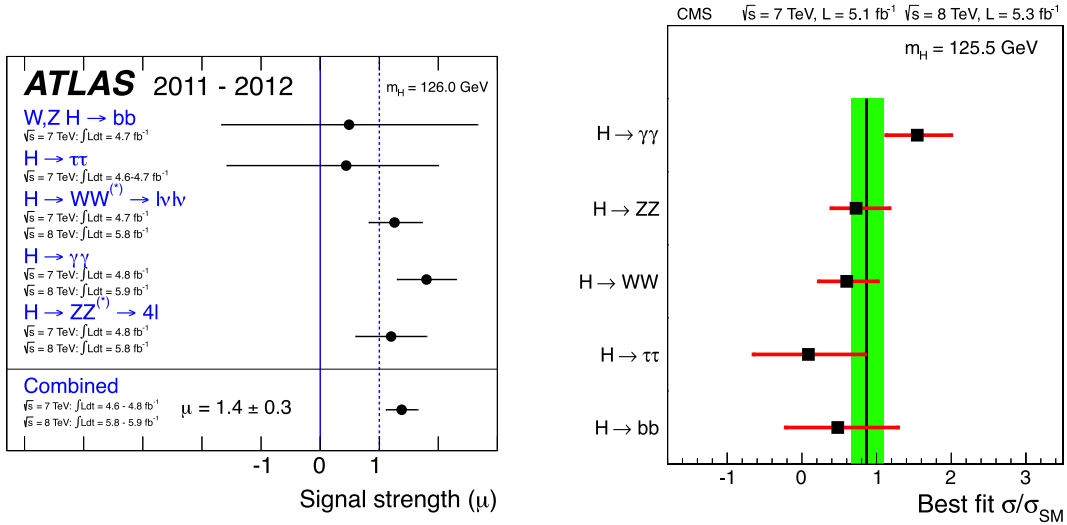
Fig. 20. The signal strength parameter for the individual channels and the combination measured by ATLAS [50] (left) and CMS [51] (right).
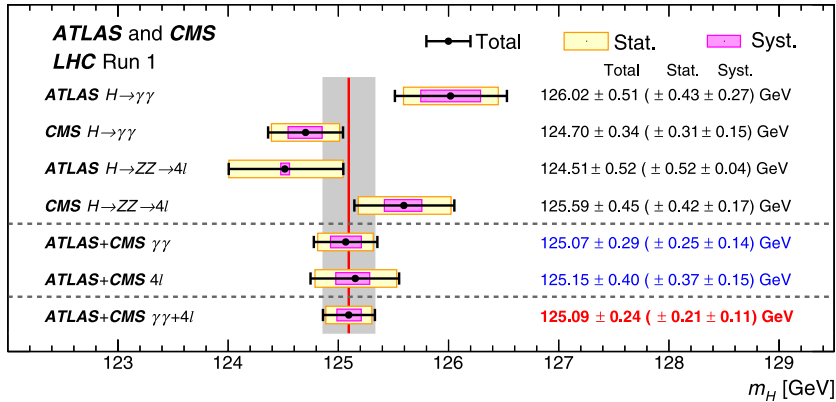

Fig. 21. Summary of the Higgs boson mass measurements from the individual analyses of ATLAS and CMS compared with the combination [52].

The combined measurement of the Higgs boson mass performed in the $H \rightarrow ZZ$ and $H \rightarrow \gamma\gamma$ channels using the LHC Run 1 data sets of the ATLAS and CMS experiments give the following result [52]:

$$m_{\mathrm{H}} = 125.09 \pm 0.24\,\mathrm{GeV}$$
$$125.09 \pm 0.21\,(\mathrm{stat.}) \pm 0.11\,(\mathrm{syst.})\,\mathrm{GeV}. \tag{80}$$

To reduce the dependence of the results on assumptions about the Higgs boson couplings three signal-strength scale factors are introduced and profiled in the fit: two factors, $\mu_{\mathrm{ggF}+t\bar{t}\mathrm{H}}^{\gamma\gamma}$ and $\mu_{\mathrm{VBF}+\mathrm{VH}}^{\gamma\gamma}$, are used to scale the signal strength in the $H \rightarrow \gamma\gamma$ channel, the third factor μ^{4l} is used to scale the signal strength in the $H \rightarrow ZZ \rightarrow 4l$ channel. The precision of the Higgs boson mass measurement is 1.9‰. For the $H \rightarrow \gamma\gamma$ channel the dominant systematic uncertainty is due to the photon energy scale. For the $H \rightarrow ZZ \rightarrow 4l$ channel the main sources of systematic uncertainties are the electron energy scale and the muon momentum scale. Nevertheless the result is dominated by the statistical contribution. A summary of the results for the ATLAS and CMS experiments from the individual analyses compared with the combination is presented in Fig. 21. The signal strength versus the Higgs boson mass shown in Fig. 22 tests in the two-dimensional space the compatibility of the measurements between the two experiments and between the different decay channels.

4.4.5. The Higgs boson charge conjugation

In the *SM*, the Higgs boson is *C*-even by construction because the Higgs field is real. A more general complex Higgs field with non-identical anti-Higgs field will require at least one additional degree of freedom e.g. two Higgs field doublets. The Higgs boson is observed in the $H \rightarrow \gamma\gamma$ channel, due to the Landau–Yang theorem one can already conclude it does not have
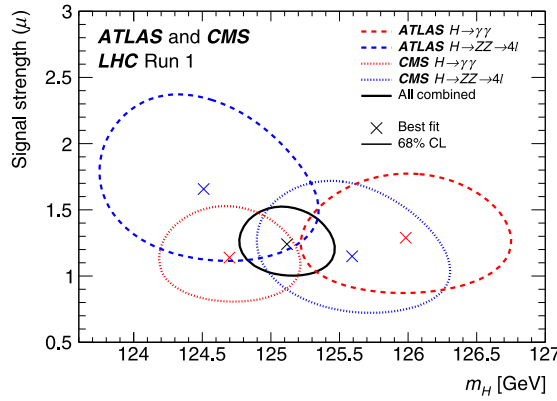
Fig. 22. Signal strength versus Higgs boson mass for the ATLAS and CMS experiments and for the $H \rightarrow ZZ \rightarrow 4l$ and $H \rightarrow \gamma\gamma$ channels [52]. The 68% C.L. confidence regions of the individual measurements are shown by the dashed curves and of the overall combination by the solid curve. The markers indicate the respective best-fit values.

spin 1. Given the photons are C-odd eigenstates, considering the charge is a multiplicative number, assuming C conservation for the decay, the observed Higgs boson should be C-even ($J^C = J^+$).

4.4.6. The Higgs boson spin and parity measurements

The *SM* Higgs boson is expected to have zero spin and positive parity quantum numbers: $J^P = 0^+$. The Higgs boson spin and parity can be studied in the $H \rightarrow ZZ$, $H \rightarrow WW$ and $H \rightarrow \gamma\gamma$ channels. Considering the production and decay process $gg(q\bar{q}) \rightarrow X \rightarrow VV \rightarrow 4f$ (Fig. 23), where X can be the *SM* Higgs boson or a more general exotic particle, five angles fully characterize the relative orientation of the decay chain:

- θ^*, the angle between the V_1–V_2 direction and the $gg(q\bar{q})$ axis;
- Φ_1, the angle between the V_1 decay plane (made by the V_1 direction and fermion direction) and the "production plane" (made by the $V_1 - V_2$ direction and the $gg(q\bar{q})$ axis);
- Φ, the angle between the V_1 and V_2 decay planes;
- θ_1, the angle between the leptons and the V_1 directions;
- θ_2, the angle between the leptons and the V_2 directions.

The five angles $\vec{\Omega}(\theta^*, \Phi_1, \theta_1, \theta_2, \Phi)$ and the invariant masses of the lepton pairs, m_{V_1} and m_{V_2}, provide significant discriminating power between signal and background, as well as between alternative signal models. Denoting with $\mathcal{T}_{\lambda 1, \lambda 2}$ the helicity amplitudes of the $V_1 V_2$ pair, the polar-angle distribution with CP-invariance approximation is [53]:

$$
\frac{d\Gamma}{d\cos\theta_1 d\cos\theta_2} \sim \sin^2\theta_1 \sin^2\theta_2 \, |\mathcal{T}_{00}|^2 + \frac{1}{2}(1+\cos^2\theta_1)(1+\cos^2\theta_2)\left[|\mathcal{T}_{11}|^2 + |\mathcal{T}_{1,-1}|^2\right]
$$
$$
+ (1+\cos^2\theta_1)\sin^2\theta_2 \, |\mathcal{T}_{10}|^2 + \sin^2\theta_1(1+\cos^2\theta_2)|\mathcal{T}_{01}|^2
$$
$$
+ 2\,\eta_1\eta_2 \cos\theta_1 \cos\theta_2 \left[|\mathcal{T}_{11}|^2 - |\mathcal{T}_{1,-1}|^2\right] \tag{81}
$$

while the general azimuthal angular distribution reads:

$$
\frac{d\Gamma}{d\Phi} \sim |\mathcal{T}_{11}|^2 + |\mathcal{T}_{10}|^2 + |\mathcal{T}_{1,-1}|^2 + |\mathcal{T}_{01}|^2 + |\mathcal{T}_{00}|^2/2
$$
$$
+ \eta_1\eta_2 \left(\frac{3\pi}{8}\right)^2 \Re e(\mathcal{T}_{11}\mathcal{T}_{00}^* + \mathcal{T}_{10}\mathcal{T}_{0,-1}^*)\cos\Phi + \frac{1}{4}\Re e(\mathcal{T}_{11}\mathcal{T}_{-1,-1}^*)\cos 2\Phi \tag{82}
$$

were $\eta_i = 2v_i a_i/(v_i^2 + a_i^2)$.

With the spin-zero hypothesis for the X particle, the two V bosons should have the same helicity ($\mathcal{T}_{10} = \mathcal{T}_{01} = \mathcal{T}_{1,-1} = 0$). The helicity amplitudes of the $H \rightarrow Z^*Z$ decay in the Standard Model are given by:

$$
\mathcal{T}_{00} = \frac{M_H^2 - M_Z^2 - M_*^2}{2M_Z M_*}, \quad \mathcal{T}_{11} = -1, \quad \mathcal{T}_{10} = \mathcal{T}_{01} = \mathcal{T}_{1,-1} = 0. \tag{83}
$$

The normality of the Higgs boson state, $n_H = (-1)^J P$, connects the helicity amplitudes under parity transformations: $\mathcal{T}_{\lambda 1, \lambda 2} = n_H \mathcal{T}_{-\lambda 1, -\lambda 2}$. For odd normality the helicity amplitude $\mathcal{T}_{00}$ must vanish and the product $\mathcal{T}_{11}\mathcal{T}_{-1,-1}^*$ increases and flips the sign (Eq. (82) and Fig. 24 left). Different spin/parity hypothesis for the X particle lead to different helicity amplitudes and consequently to different polar and azimuthal angular distributions. The process $gg(q\bar{q}) \rightarrow X \rightarrow \gamma\gamma$ can be used to improve
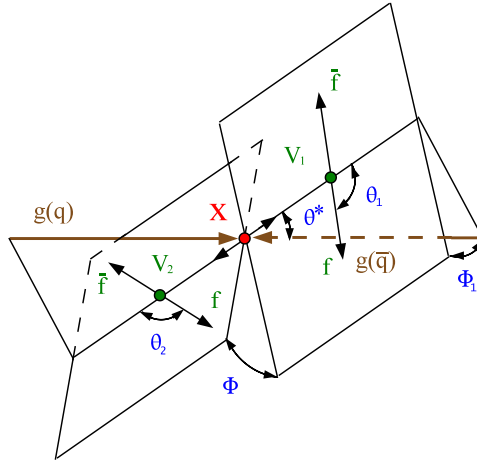
Fig. 23. Illustration of the $gg(q\overline{q}i\overline{t}) \rightarrow H \rightarrow V_1V_2 \rightarrow 4f$ production process and decay channel with the five angles $\vec{\Omega}(\theta^*, \Phi_1, \theta_1, \theta_2, \Phi)$ described in the text.
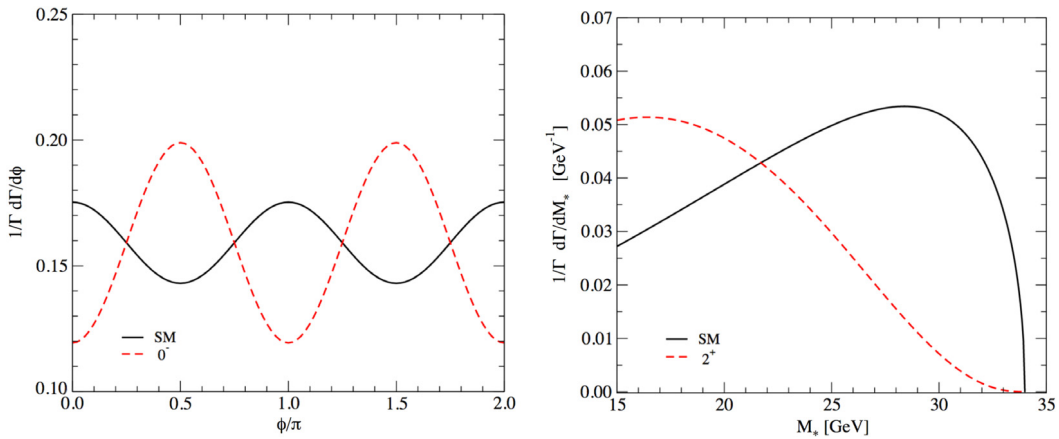

Fig. 24. Distributions of some variables for the $H \rightarrow Z^*Z$ decay with $m_H = 125$ GeV [54]. Azimuthal angular distribution between the two Z decay planes for spin $= 0$ with positive parity in the *SM* compared with negative parity (left); M_* distribution for the *SM* and spin-2 even normality bosons (right).

the discrimination of the spin two models. The state $J^P = 0^+$ is assumed to be the *SM* Higgs boson or at least a scalar with the same coupling structure to gluons, fermions and V bosons. The definitions of the coupling structure of the pseudo-scalar state $J^P = 0^-$, the exotic vector $J^P = 1^-$, the exotic axial–vector $J^P = 1^+$, the tensor $J^P = 2^+$ and the pseudo-tensor $J^P = 2^-$ can be found in Ref. [55]. Fig. 25 shows the test statistic $\tilde{q} = -2\ln(\mathcal{L}_{0^- +\text{bkg}}/\mathcal{L}_{0^+ +\text{bkg}})$ for the signal hypothesis 0^- and 0^+ added to the background. The ATLAS experiment performed the analysis with the $H \rightarrow ZZ, H \rightarrow WW$ decay channels and excluded the pseudo-scalar state $J^P = 0^-$ compatibility with C.L. < 0.026% [56]. The CMS experiment performed the analysis with the $H \rightarrow ZZ$ decay channel and excluded the $J^P = 0^-$ hypothesis with C.L. = 0.05% [58]. The test statistic for the axial–vector state 1^+ and for the graviton tensor state 2^+ are shown in Fig. 26. The QCD production of a spin-2 particle is driven by the values of the couplings k_g, k_q. The gluon fusion production $gg \rightarrow X$ ($k_q = 0$) and the universal coupling scenario ($k_g = k_q$) are shown in Fig. 26 (center and right).

The results of the test statistic for additional models can be found for ATLAS in Ref. [56,59] and for CMS in Ref. [57,58]. In the ATLAS analysis, for the 2^+ graviton-like tensor hypothesis, when $k_g \neq k_q$ a cut on p_T^X is applied to remove the high p_T^X tail where the effective field theory (EFT) is not valid (soft selection $p_T^X < 300$ GeV, hard selection $p_T^X < 125$ GeV). Table 7 is a summary of the main J^P test statistic made by the ATLAS and CMS experiments for different models. All the models are disfavored with respect to the *SM* Higgs boson state $J^P = 0^+$ with a C.L. always lower than 4.5%.

4.4.7. The Higgs boson signal strength and coupling modifiers measurements

The measurements of the signal strengths and of the coupling modifiers introduced in Section 4.2 are obtained by fitting the observed event yields. To increase the number of measurable coupling modifiers or to improve the precision of the fit, all the accessible decay channels and production modes must be considered. These measurements are important to test the
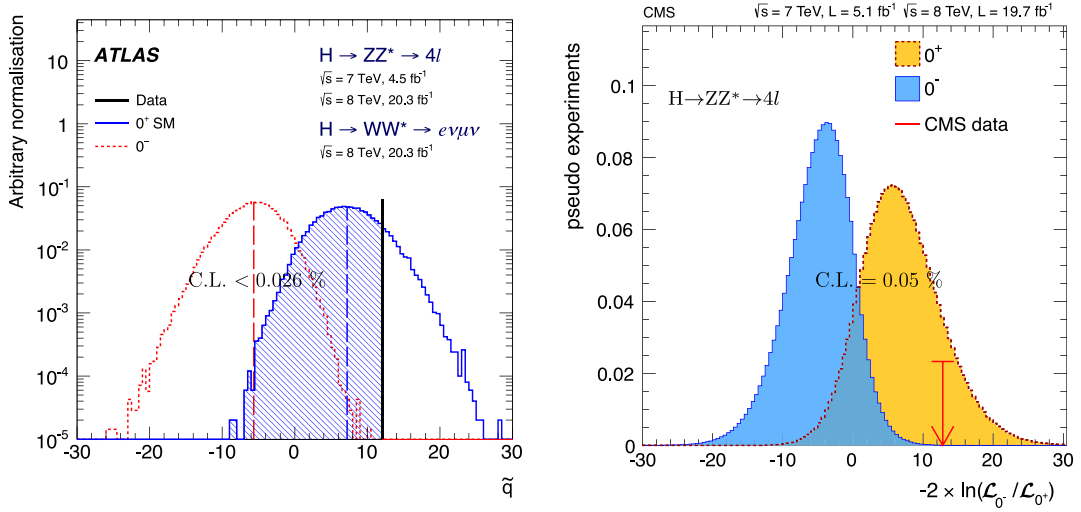
Fig. 25. The test statistic for the pseudo-scalar state $J^P = 0^-$ made with the likelihood ratio $\tilde{q} = -2\ln(\mathcal{L}_{0^- +bkg}/\mathcal{L}_{0^+ +bkg})$. The distribution of pseudo experiments for ATLAS [56] (left) and CMS [57] (right).
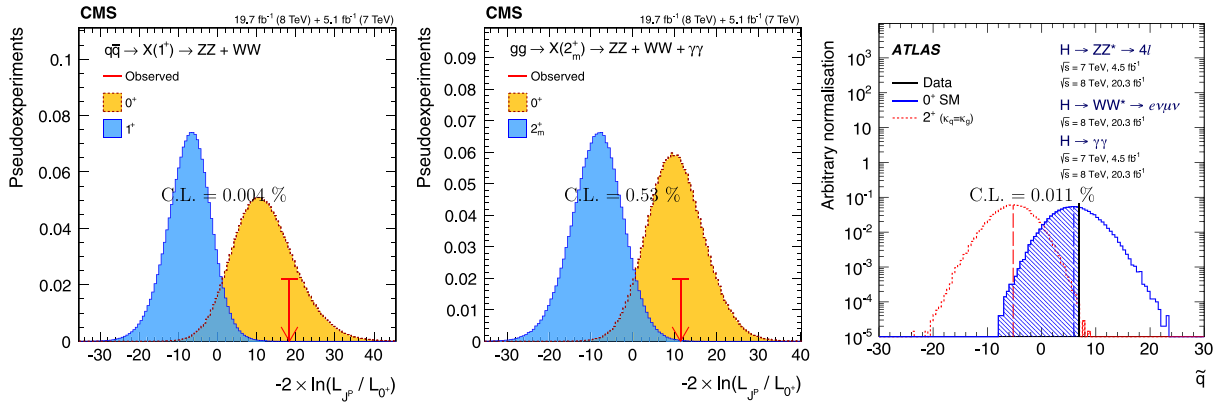

Fig. 26. The test statistic for: the axial–vector state $J^P = 1^+$ at CMS [58] (left), the graviton-like tensor state $J^P = 2^+$ with gluon–gluon fusion at CMS [58] (center), the graviton-like tensor state $J^P = 2^+$ with the universal coupling scenario at ATLAS [56] (right).

Table 7
Results of the J^P test statistic made by the ATLAS and CMS experiments for different models.

Scenario	X production	Comment	C.L. (ATLAS)	C.L. (CMS)
0_h^+	Any	Scalar with higher-dimension operators	0.047% [56]	4.5% [57]
0^-	Any	Pseudo-scalar	<0.026% [56]	0.05% [57]
1^+	$q\bar{q} \to X$	Exotic axial–vector	0.03% [59]	0.004% [58]
1^-	$q\bar{q} \to X$	Exotic vector	0.27% [59]	<0.001% [58]
2_m^+ (gg)	$gg \to X$	Graviton-like tensor	0.015% [56]$_{sel.}^{hard}$	0.53% [58]
2_m^+ (UC)	$gg, q\bar{q} \to X$	Graviton-like tensor	0.011% [56]	
2_h^+ (gg)	$gg \to X$	Tensor with higher-dimension operators		1.9% [58]
2_h^- (gg)	$gg \to X$	Pseudo-tensor		0.039% [58]

compatibility of the new resonance with the *SM* Higgs boson. The separation between different production modes can be obtained with specific tags described in Fig. 27. The uncertainty of the separation between a specific production process and the dominant gluon–gluon fusion process depends to the selection cuts, the considered process and the considered Higgs boson decay. Considering the five main decay channels $H \to ZZ$, $H \to WW$, $H \to \gamma\gamma$, $H \to \tau\tau$ and $H \to b\bar{b}$ and the five
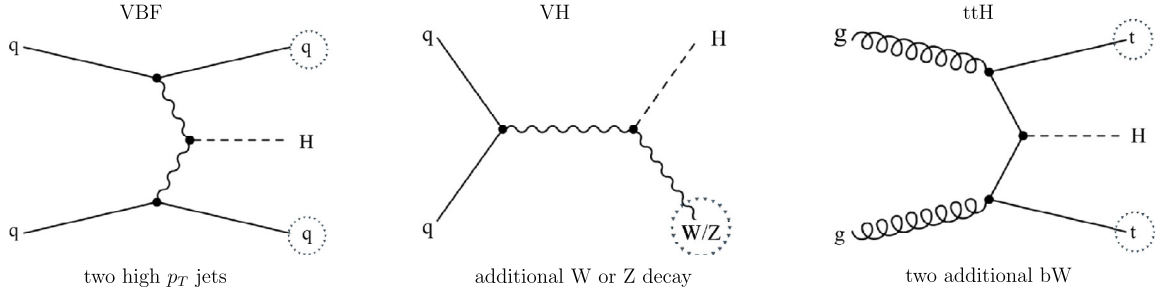
Fig. 27. Description of the tags for the selection of different Higgs boson production channels: *VBF* is selected with the requirement of two high p_T jets with high pseudorapidity separation; *VH* is selected with the requirement of one additional vector boson; *ttH* is selected with the requirement of two additional *bW* arising from the two top quark decays.

Table 8
The signal parameterization used to express the $\sigma_i \cdot BR^f$ values for each specific channel $i \rightarrow H \rightarrow f$. The values labeled with a "–" are not probed and are therefore fixed to the *SM* predictions.

Production process	Decay channel				
	$H \rightarrow \gamma\gamma$	$H \rightarrow ZZ$	HWW	$H \rightarrow \tau\tau$	$H \rightarrow bb$
ggF	$(\sigma \cdot BR)^{\gamma\gamma}_{ggF}$	$(\sigma \cdot BR)^{ZZ}_{ggF}$	$(\sigma \cdot BR)^{WW}_{ggF}$	$(\sigma \cdot BR)^{\tau\tau}_{ggF}$	–
VBF	$(\sigma \cdot BR)^{\gamma\gamma}_{VBF}$	$(\sigma \cdot BR)^{ZZ}_{VBF}$	$(\sigma \cdot BR)^{WW}_{VBF}$	$(\sigma \cdot BR)^{\tau\tau}_{VBF}$	–
WH	$(\sigma \cdot BR)^{\gamma\gamma}_{WH}$	$(\sigma \cdot BR)^{ZZ}_{WH}$	$(\sigma \cdot BR)^{WW}_{WH}$	$(\sigma \cdot BR)^{\tau\tau}_{WH}$	$(\sigma \cdot BR)^{bb}_{WH}$
ZH	$(\sigma \cdot BR)^{\gamma\gamma}_{ZH}$	$(\sigma \cdot BR)^{ZZ}_{ZH}$	$(\sigma \cdot BR)^{WW}_{ZH}$	$(\sigma \cdot BR)^{\tau\tau}_{ZH}$	$(\sigma \cdot BR)^{bb}_{ZH}$
ttH	$(\sigma \cdot BR)^{\gamma\gamma}_{ttH}$	$(\sigma \cdot BR)^{ZZ}_{ttH}$	$(\sigma \cdot BR)^{WW}_{ttH}$	$(\sigma \cdot BR)^{\tau\tau}_{ttH}$	$(\sigma \cdot BR)^{bb}_{ttH}$

production processes ggF, VBF, WH, ZH, and ttH there are in principle 25 independent products to be measured. The $H \rightarrow \mu\mu$ channel is not considered due to its very low sensitivity. In case of the $H \rightarrow b\bar{b}$ decay channel the *ggF* and VBF production processes are not probed, we can assume the values predicted by the SM. In truth CMS published an analysis for the $H \rightarrow b\bar{b}$ channel produced through VBF [60] but only with the $\sqrt{s} = 8$ TeV data sample and with the expected significance of 0.8. The 23 parameters to be fitted are shown in Table 8.

The analysis of these 5 decays channels made by the ATLAS and CMS experiments have been combined together [61]. Every single analysis measured the signal significance and the signal strength but there are some differences in the treatment of signal and background between the two experiments or between different channels. In the combined analysis there is a common mass $m_H = 125.09$ GeV and a common global fit including all the channels. The best fit values of the $\sigma_i \cdot B^f$ parameters are shown in Fig. 28 (left). Only 20 parameters are shown because for the $H \rightarrow ZZ$ decay channel, the ZH, WH, and ttH production processes cannot be measured with meaningful precision. Assuming the *SM* values for the Higgs boson branching fractions $BR^f = (BR^f)_{SM}$ and combining the different decays channels the production signal strength $\mu_i = \sigma_i/(\sigma_i)_{SM}$ is derived, the best fit results are shown in Fig. 28 (right). Similarly assuming that the Higgs boson production cross sections are the same as in the *SM* the decay signal strength $\mu^f = BR^f/(BR^f)_{SM}$ is derived. All the signal strengths with the previous assumptions are compatible with 1 and the two experiments have compatible individual results. The simplest and most restrictive parameterization is to assume that the values of the signal strengths are the same for all production processes and decay channels. The measured inclusive signal strength is:

$$\mu_{incl.} = 1.09 \pm 0.07(\text{stat.}) \pm 0.08(\text{syst.}) \tag{84}$$

The systematic uncertainty is larger than the statistical uncertainty and its largest component is the theoretical uncertainty in the *ggF* cross section. As discussed in Section 4.2 if $\Gamma_H = (\Gamma_H)_{SM}$ the signal strength is the product of the coupling modifiers $\mu^f_i = k^2_i k^2_f$ and k^2_i, k^2_f can be extrapolated with the ratio between two signal strengths having the same production processes but different decays or the same decays but different production processes. More generally, an assumption about the Higgs boson width is necessary. It should be reminded that changes in the values of the couplings will result in a variation of the Higgs boson width. If the Higgs boson can decay only in the known particles but with different partial widths with respect to the *SM* values, the change in the total width will be:

$$\Gamma^{SM}_H = \sum_j \Gamma^{SM}_j = \sum_j B_{jSM} \Gamma^{SM}_H \implies \Gamma_H = \sum_j \Gamma_j = \sum_j k^2_j B_{jSM} \Gamma^{SM}_H = k^2_H \Gamma^{SM}_H \tag{85}$$

where $k^2_H = \sum_j k^2_j B_{jSM}$ is the modifier to the total width due to the known particles. If the Higgs boson can decay also in particles beyond the Standard Model (BSM) with a branching fraction B_{BSM} the total width must be increased by a factor
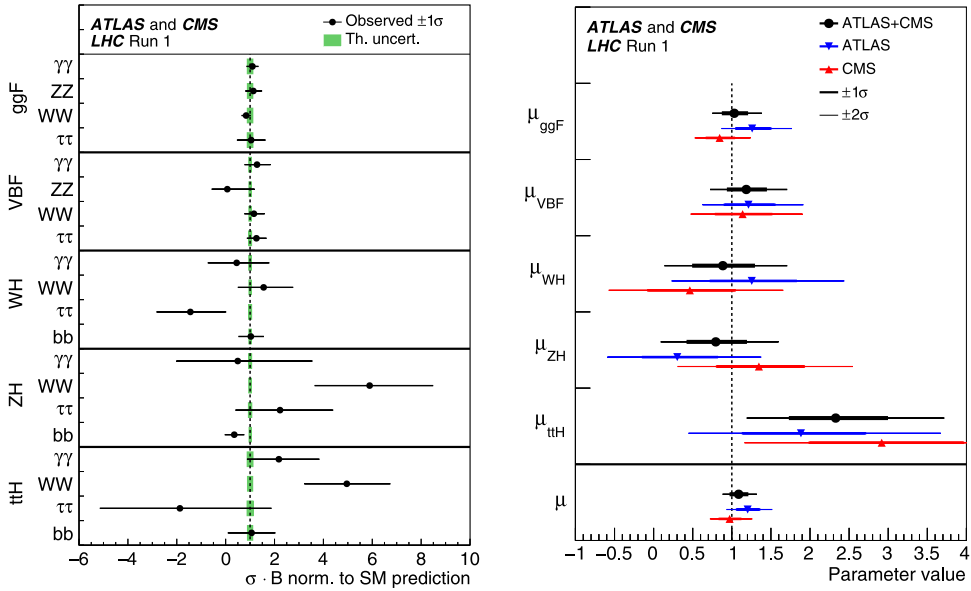
Fig. 28. Best fit values of the signal strength $\mu_i^f = \sigma_i \cdot BR^f / (\sigma_i)_{SM} \cdot (BR^f)_{SM}$ for the ATLAS and CMS combination [61]. The error bars indicate the 1σ intervals. The shaded bands indicate the theoretical uncertainties in the *SM* predictions (left). Best fit results for the production signal strengths $\mu_i = \sigma_i/(\sigma_i)_{SM}$ for ATLAS, CMS and their combination assuming the *SM* values for the Higgs boson branching fractions. The error bars indicate the 1σ and 2σ intervals. The measurements of the global signal strength are also shown (right).

Table 9
The fit results of the coupling modifiers in the $B_{BSM} \neq 0$ scenario with their uncertainties for the ATLAS and CMS combination [61].

k_Z	k_W	k_t	$|k_\tau|$	$|k_b|$	$|k_g|$	$|k_\gamma|$	B_{BSM}
$1^{+0}_{-0.08}$	$0.9^{+0.09}_{-0.09}$	$1.43^{+0.23}_{-0.22}$	$0.87^{+0.12}_{-0.11}$	$0.57^{+0.16}_{-0.16}$	$0.81^{+0.13}_{-0.10}$	$0.9^{+0.10}_{-0.09}$	$0^{+0.16}$

$1/(1 - B_{BSM})$:

$$\Gamma_H = \frac{k_H^2 \Gamma_H^{SM}}{1 - B_{BSM}} \tag{86}$$

Two possible scenarios have been considered:

(1) $B_{BSM} \geq 0$ with $|k_V| \leq 1$ and sign(k_Z) = sign(k_W);
(2) $B_{BSM} = 0$.

The constraints assumed in the first scenario are compatible with a wide range of BSM physics, which may become manifest in the $gg \rightarrow H$ and $H \rightarrow \gamma\gamma$ loop-induced processes. The potential deviations from the *SM* of the tree-level couplings to ordinary particles are parameterized with their respective coupling modifiers. The parameters of interest in the fits to data are the seven independent coupling modifiers one for each particle involved in the production processes and decay modes:

$$k_Z, \quad k_W, \quad k_t, \quad k_\tau, \quad k_b, \quad k_g \quad \text{and} \quad k_\gamma \tag{87}$$

where k_g and k_γ are the effective coupling modifiers which describe loop processes for the $gg \rightarrow H$ production and $H \rightarrow \gamma\gamma$ decay. In the case of the first scenario, the additional parameter B_{BSM} is considered in the fit. Fig. 29 shows the fit results for the two scenarios. Other possible scenarios have been considered and fitted in Ref. [61]. The fitted parameters for the first scenario are reported in Table 9. All the modifiers $|k_j|$ are compatible with 1 within 2σ (with the exception of $|k_b|$ with a deviation of 2.7σ) and B_{BSM} is compatible with 0 but the errors are still high, of the order of 10–20%. Starting from the identities of the coupling between the Higgs boson and fermions $g_{Hff} = m_F/v$ (Eq. (49)) and the coupling between the Higgs boson and vector bosons $g_{HWW} = 2 m_W^2/v$, $g_{HZZ} = m_Z^2/v$ (Eq. (46)) the following new parameters can be introduced:

$$k_F \, g_{Hff} = k_F \, m_F/v \qquad \sqrt{k_W \, g_{HWW}/2v}, \quad \sqrt{k_Z \, g_{HZZ}/v} = \sqrt{k_V} \, m_V/v \tag{88}$$

The plot of these parameters as a function of the particle mass gives a linear relation between couplings and masses with a view of the potential deviation from the linear trend produced by the coupling modifiers. The best fit values of the parameters
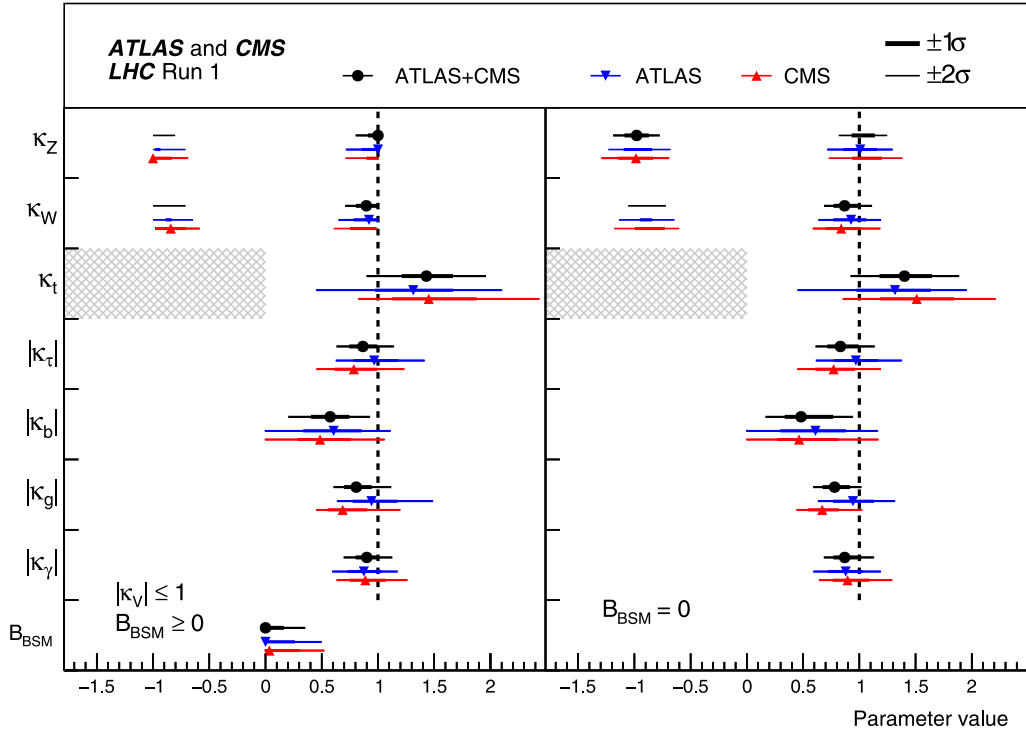
Fig. 29. Fit results for two parameterizations: the first one assumes $B_{BSM} \geq 0$ with $|k_V| \leq 1$, the second one assumes $B_{BSM} = 0$. The fit results of the ATLAS and CMS experiments are reported together with their combinations [61]. The hatched areas show the non-allowed regions for the k_t parameter, which is assumed to be positive without loss of generality. The error bars indicate the 1σ and 2σ intervals. When a parameter is constrained and reaches a boundary, the uncertainty is not defined beyond this boundary. For those parameters with no sensitivity to the sign, only the absolute values are shown.
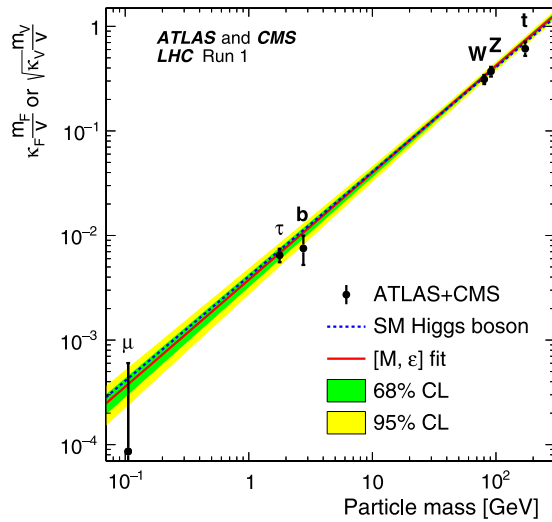

Fig. 30. Best fit values of the parameters defined as $k_F m_F/v$ for the fermions, and as $\sqrt{k_V} m_V/v$ for the weak vector bosons as a function of the particle mass, where $v = 246$ GeV is the vacuum expectation value of the Higgs field [61]. The dashed line indicates the predicted dependence on the particle mass in the case of the *SM* Higgs boson. The solid line indicates the best fit result to the $[M, \epsilon]$ parameters of the phenomenological model of Ref. [62].

in the $B_{BSM} = 0$ scenario are shown in Fig. 30 as a function of the particle mass. The results of the $H \rightarrow \mu\mu$ analysis are included for this specific case.

All measurements based on the generic parameterizations are compatible between the two experiments and with the predictions of the SM. The potential presence of physics beyond the Standard Model is also probed using specific
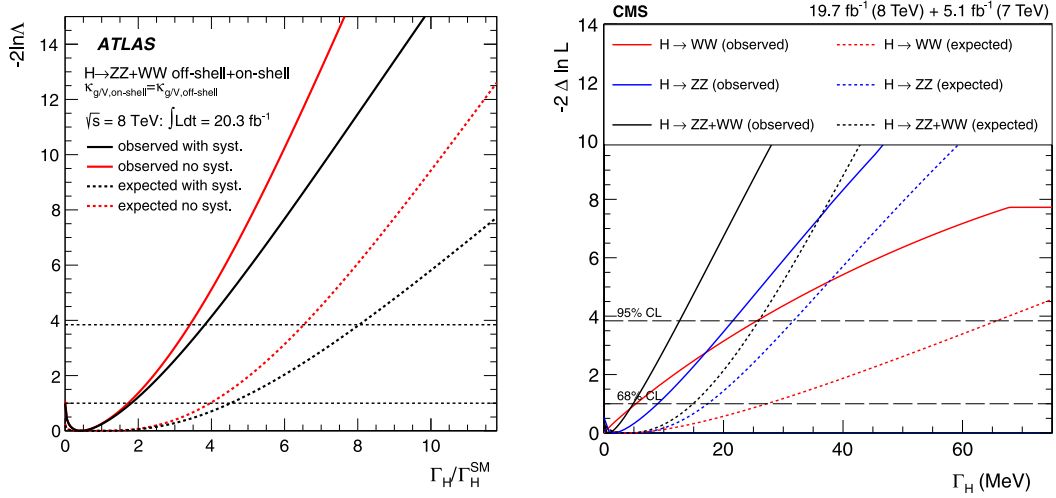
Fig. 31. The ATLAS result on the Higgs boson width limit [63] (left). The CMS result on the Higgs boson width limit with the $\mu_{gg}^{ZZ}/\mu_{gg}^{WW} = \mu_{VBF}^{ZZ}/\mu_{VBF}^{WW}$ assumption [64] (right). The plots are the scan of the log-likelihood as a function of the Higgs boson width. The solid lines are the observed log-likelihood, the dashed lines are the expected one.

parameterizations, the overall branching fraction of the Higgs boson into BSM decays is determined to be less than 34% at 95% C.L.

4.4.8. The Higgs boson width limit

The direct measurement of the Higgs boson width is not possible at a hadron collider due to the limited experimental resolution of the invariant mass, about three order of magnitude larger than the expected *SM* Higgs boson width of 4 MeV (Fig. 5). An alternative solution is to constrain the Higgs boson width by comparing the on-shell with the off-shell cross sections. The cross section for the $H \to VV$ process is expected to have the Breit–Wigner shape:

$$\frac{d\sigma}{dM_{VV}} = \sigma_H \frac{M_H \Gamma_H}{\pi} \frac{2M_{VV}}{\left(M_{VV}^2 - M_H^2\right)^2 + (M_H \Gamma_H)^2} \ , \tag{89}$$

which close to the Higgs boson mass peak and for the dominant gluon–gluon fusion production mode can be expressed as:

$$\left(\frac{d\sigma}{dM_{VV}}\right)_{\text{on-shell}} \sim \frac{g_{ggH}^2 \, g_{HVV}^2}{M_H \Gamma_H} \tag{90}$$

Therefore in order to measure the Higgs boson couplings one must either first measure the width, or measure the couplings under the assumption of a known total width. In the phase space region away from the Higgs boson resonance Eq. (90) is no longer valid, since the Higgs boson propagator is dominated by the $(M_{VV}^2 - M_H^2)$ term and the cross section is essentially independent of the width:

$$\left(\frac{d\sigma}{dM_{VV}}\right)_{\text{off-shell}} \sim g_{ggH}^2 \, g_{HVV}^2 \tag{91}$$

Dividing the cross sections by the *SM* expectations the couplings are replaced with the coupling modifiers. With the assumption that the coupling modifiers are the same in the on-shell and off-shell regions $kj^{\text{on-shell}} = kj^{\text{off-shell}}$ is possible to constrain the Higgs boson width. The off-shell analysis made by ATLAS to constrain the Higgs boson width used the data sample recorded in 2012 at $\sqrt{s} = 8$ TeV and the $ZZ \to 4\ell$, $ZZ \to 2\ell 2\nu$ and $WW \to e\nu\mu\nu$ final states [63]. The off-shell analysis made by CMS used the Run 1 data sample and the same final states [64]. The results on the Higgs boson width limit from ATLAS and CMS are shown in Fig. 31 in terms of log-likelihood scan as a function of the Higgs boson width. The crossing of the observed line with the corresponding 95% C.L. of the log-likelihood gives the width limit. The observed limits are shown in Table 10 for the separate channels and for the combination. The precise determination of the Higgs boson mass is important because the limit is measured for the ratio Γ_H/Γ_H^{SM} and 0.2% of variation for m_H corresponds to a variation of 1% for Γ_H^{SM}. In the ATLAS analysis Γ_H^{SM} is assumed to be 4.12 MeV, in the CMS analysis is assumed to be 4.15 MeV.

4.5. Higgs boson searches at LHC with collision data at $\sqrt{s} = 13$ TeV

In June 5th 2015, after 27 months of long stop necessary to repair the magnets, LHC restarted with a new energy record of $\sqrt{s} = 13$ TeV. The integrated luminosities delivered to the ATLAS and CMS experiments were about 4 fb^{-1} in the second

Table 10

Limits for the Higgs boson width at 95% of C.L. measured by ATLAS [63] and CMS [64] for the *ZZ* and *WW* channels and for the combination. The value in parenthesis for CMS is the limit obtained by relaxing the $\mu_{gg}^{ZZ}/\mu_{gg}^{WW} = \mu_{VBF}^{ZZ}/\mu_{VBF}^{WW}$ assumption.

	ZZ	*WW*	combination
ATLAS	–	–	$\Gamma_H < 22.7$ MeV
CMS	$\Gamma_H < 22$ MeV	$\Gamma_H < 26$ MeV	$\Gamma_H < 13$ MeV (15 MeV)

Table 11

The integrated luminosities delivered by LHC and recorded by the ATLAS and CMS experiments in the Run 1 (2011, 2012) and Run 2 (2015, 2016, 2017). The last column is the fraction of the data recorded considered good for physics.

Year	$\sqrt{s}$ (TeV)	ATLAS			CMS		
		Delivered (fb^{-1})	Recorded (fb^{-1})	Physics (fb^{-1})	Delivered (fb^{-1})	Recorded (fb^{-1})	Physics (fb^{-1})
2011	7	5.5	5.1	4.5	6.1	5.5	5.1
2012	8	22.8	21.3	20.3	23.3	21.8	19.7
2015	13	4.2	3.9	3.2	4.2	3.8	2.3
2016	13	38.5	35.6	32.9	40.8	37.8	35.9
2017	13	50.4	47.1	~44	51.0	46.0	~43

Table 12

Higgs boson mass and signal strength measurements. The ATLAS+CMS Run 1 combination [52] is compared with the preliminary ATLAS and CMS Run 2 measurements with a data sample corresponding to an integrated luminosity of ~36 fb^{-1} [65–69]. The last column shows the specific decays channel, or the channel combination, used for each measurement.

Data sample	Integrated luminosity	m_H		μ	
Run 1 ATLAS+CMS	~25 fb^{-1} + 25 fb^{-1}	125.09 ± 0.24	(1), (2)	$1.09^{+0.11}_{-0.10}$	(1)–5)
Run 2 CMS 2016	~36 fb^{-1}	125.26 ± 0.21	(1)	$1.05^{+0.19}_{-0.17}$	(1)
		125.40 ± 0.33	(2)	$1.16^{+0.15}_{-0.14}$	(2)
Run 2 ATLAS 2015+2016	~36 fb^{-1}	124.88 ± 0.37	(1)	$1.24^{+0.19}_{-0.19}$	(1)
		125.11 ± 0.42	(2)	$0.99^{+0.14}_{-0.14}$	(2)
		124.98 ± 0.28	(1), (2)	$1.09^{+0.12}_{-0.12}$	(1), (2)

(1) $H \rightarrow ZZ$　　(2) $H \rightarrow \gamma\gamma$　　(3) $H \rightarrow WW$　　(4) $H \rightarrow \tau\tau$　　(5) $H \rightarrow b\bar{b}$

half of 2015, ~40 fb^{-1} in 2016 and ~50 fb^{-1} in 2017. Table 11 shows the summary of the integrated luminosities delivered, recorded and good for physics in the Run 1 (2011, 2012) and Run 2 (2015, 2016, 2017). The fractions Recorded/Delivered and Physics/Recorded are different year by year but always of the order of 90–95%.

The first step was rediscovering the Higgs boson at $\sqrt{s} = 13$ TeV, the second step will be to remeasure all the Higgs boson properties with higher precision using the full $\sqrt{s} = 13$ TeV data sample. To complete and to combine all the analysis it will require some time, meanwhile some results with a partial statistics have been presented to the conferences, only few Higgs boson searches have been published.

4.5.1. Higgs boson mass and signal strength measurements

The ATLAS and CMS experiments presented at the EPS-HEP 2017 conference, among several other preliminary results using $\sqrt{s} = 13$ TeV data samples, the measurement of properties of the Higgs bosons with the decay channels $H \rightarrow ZZ \rightarrow 4l$ and $H \rightarrow \gamma\gamma$ [65–69]. The ATLAS analysis used the integrated luminosity of 36.1 fb^{-1} recorded in 2015 and 2016. The CMS analysis used the integrated luminosity of 35.9 fb^{-1} recorded in 2016. Fig. 32 shows for the ATLAS and CMS experiments the four-lepton and the $\gamma\gamma$ invariant mass distributions for the selected candidates compared to the expected signal and background contributions. The Higgs boson mass measured by CMS with the 4l channel is $m_H = 125.26 \pm 0.21$ GeV, the Higgs boson mass measured by ATLAS with the 4l + $\gamma\gamma$ channels is $m_H = 124.98 \pm 0.28$ GeV. The signal strengths were measured separately for the 4l and the $\gamma\gamma$ channels. Table 12 shows the measurements of the Higgs boson mass and signal strength comparing the results of the Run 1 combination with the Run 2 measurements. The Run 2 preliminary results are already competitive with the Run 1 combination. The different Higgs boson mass and signal strength measurements are compatible between them and the signal strength measurements are compatible with the *SM* expectation. The errors are dominated by the statistical uncertainty.

4.5.2. $H \rightarrow b\bar{b}$ decay channel

While the Higgs boson decaying into vector bosons is an evidence since 2012 and the analysis using this decay channel are now providing detailed measurements, direct evidence of the Higgs boson to fermions was established only via the observation of the decay into τ-leptons [61,73]. For the $b\bar{b}$ decay the very large backgrounds arising from multi-jets
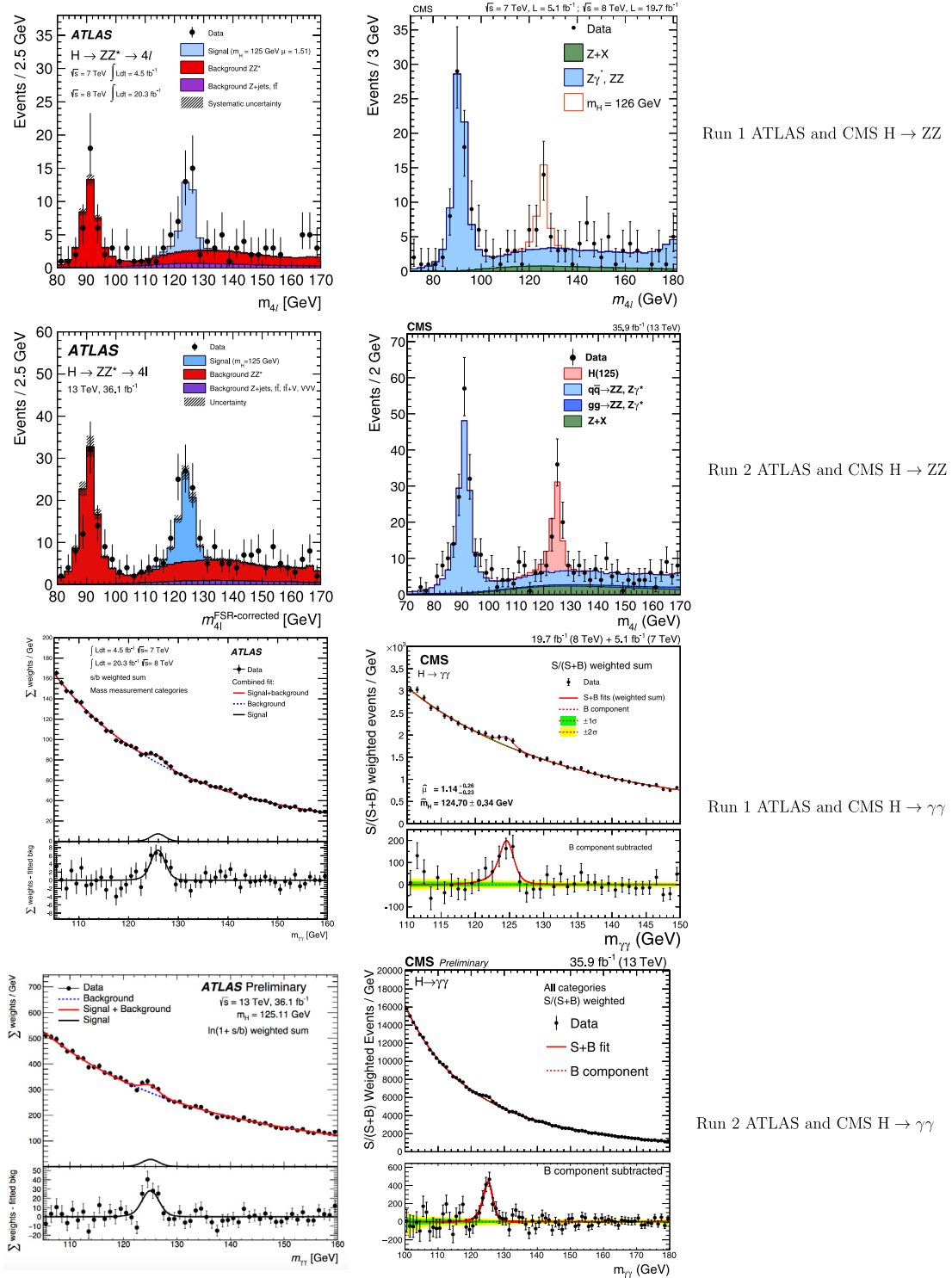
Fig. 32. Invariant mass distribution of the $H \rightarrow ZZ \rightarrow 4l$ and $H \rightarrow \gamma\gamma$ decay channel for the ATLAS and CMS experiments for the Run 1 data [57,70–72] and the Run 2 data [65,66,68,69]. The signal expectations in the different analysis are plotted with their different best fit of the Higgs boson mass and signal strength.

production make the inclusive search challenging, the most sensitive production mode is the vector boson associated production *VH*. Searches Higgs boson decay in the $b\bar{b}$ channel were reported by the ATLAS and CMS experiments with the
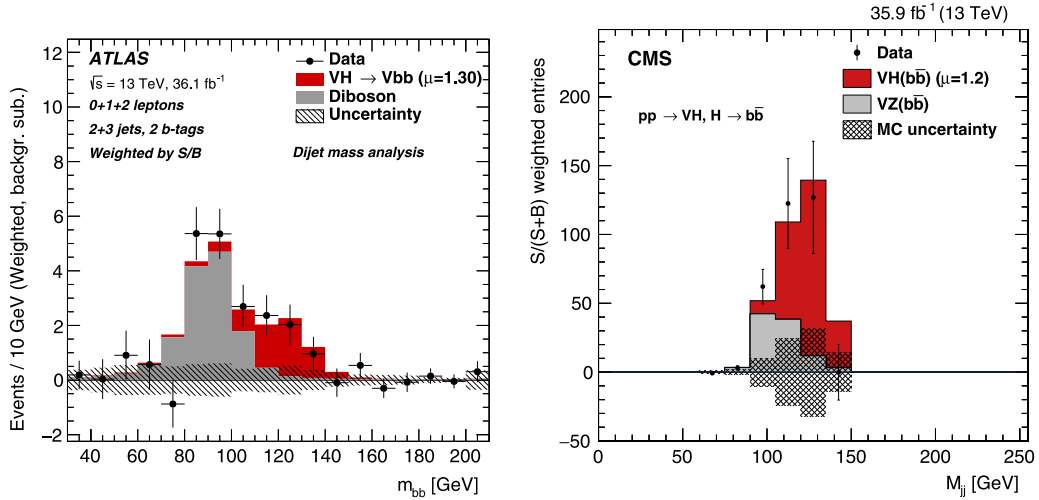
Fig. 33. The invariant mass distribution of b-tagged jets for ATLAS [74] (left) and CMS [75] (right). The data and the expected *VH* and *VZ* contributions are shown, the other backgrounds are subtracted. All the decay channels and categories are combined. The signal expectations are plotted with their best fit of the Higgs boson mass and signal strength (from the dijet-mass analysis for ATLAS and from the BDT analysis for CMS).

Table 13
The significance of the expected and observed excess of the signal for the $H \to b\bar{b}$ decay channel and the observed signal strength μ measured by the ATLAS and CMS experiments with the Run1 data [61], the Run 2 data [74] [75] and their combination.

	ATLAS			CMS		
	Significance expected	Significance observed	μ observed	Significance expected	Significance observed	μ observed
Run 1	2.7	1.7	$0.62^{+0.37}_{-0.37}$	2.5	2.0	$0.81^{+0.45}_{-0.43}$
Run 2	3.0	3.5	$1.2^{+0.42}_{-0.36}$	2.8	3.3	$1.19^{+0.40}_{-0.38}$
Run1 and Run2	4.0	3.6	$0.9^{+0.28}_{-0.26}$	3.8	3.8	$1.06^{+0.31}_{-0.29}$

Run 1 data in the *VH*, *VBF* and *ttH* associated production [61]. The observed (expected) significances were 1.7 σ (2.7 σ) for ATLAS and 2.0 σ (2.5 σ) for CMS. Recent analysis from ATLAS [74] and CMS [75] with data samples corresponding to an integrated luminosity of about 36 fb^{-1} collected in the Run 2 reported the observation of the Higgs boson decaying to $b\bar{b}$ when produced in association with a vector boson. The considered decays for the vector bosons are $Z \to \nu\nu$ (0-lepton channel), $W \to l\nu$ (1-lepton channel) and $Z \to ll$ (2-lepton channel). The event counting is performed separately for the different vector boson decays and for different p_T^V and n-jet categories. The p_T^V observable corresponds to E_{miss}^T in the 0-lepton channel, to the vectorial sum of E_{miss}^T and to the charged lepton's transverse momentum in the 1-lepton channel, and the transverse momentum of the 2-lepton system in the 2-lepton channel. Every p_T^V category is subdivided in 2-jet and 3-jet sub-categories. To separate signal from background multivariate discriminants making use of boosted decision trees (BDTs) are constructed. The ATLAS experiment performed also a dijet-mass analysis where the BDT discriminant is replaced by the $m_{b\bar{b}}$ variable as the main input used in the global fit. The distributions of the $b\bar{b}$ invariant mass are shown in Fig. 33 for the ATLAS and CMS experiments. All the decay channels and categories are combined into a weighted invariant mass plot.

The significance of the observed (expected) excess is 3.5 (3.0) standard deviation for ATLAS and 3.3 (2.8) standard deviation for CMS. The measured signal strengths and the expected and observed significances are reported in Table 13 for the ATLAS and CMS experiments, for the Run 1 analysis, for Run 2 BDT analysis and for their combination.

4.5.3. Associated production of the Higgs boson with a top quark pair ($t\bar{t}H$)

The Yukawa interaction between the Higgs boson and the top quark can be indirectly measured using the top quark contribution to gluon–gluon fusion production and diphoton decay loops. This Yukawa interaction can be directly measured with the selection of the $t\bar{t}H$ production channel. The ATLAS and CMS experiments measured with the Run 1 data the $t\bar{t}H$ production cross section for the $H \to \gamma\gamma$, $H \to WW$, $H \to \tau\tau$ and $H \to bb$ decays, the combination of these results yields a best fit of the signal strength $\mu = \sigma/\sigma_{SM}$ of $2.3^{+0.7}_{-0.6}$ [61]. The combined measured significance for the $t\bar{t}H$ process was 4.4 σ, whereas only 2.0 σ was the expected significance. To confirm this slight excess in the $t\bar{t}H$ production cross section the precision of the measurement must be improved. Recently the ALTAS experiment measured the $t\bar{t}H$ production cross section with a Run 2 data sample corresponding to an integrated luminosity of 36.1 fb^{-1} [76]. Seven multilepton final states, targeting Higgs boson decays to WW, $\tau\tau$ and ZZ categorized by the number and flavor of charged-lepton candidates, have been analyzed. Fig. 34 (left) shows the data, background and signal yields, where the final-discriminant bins in all
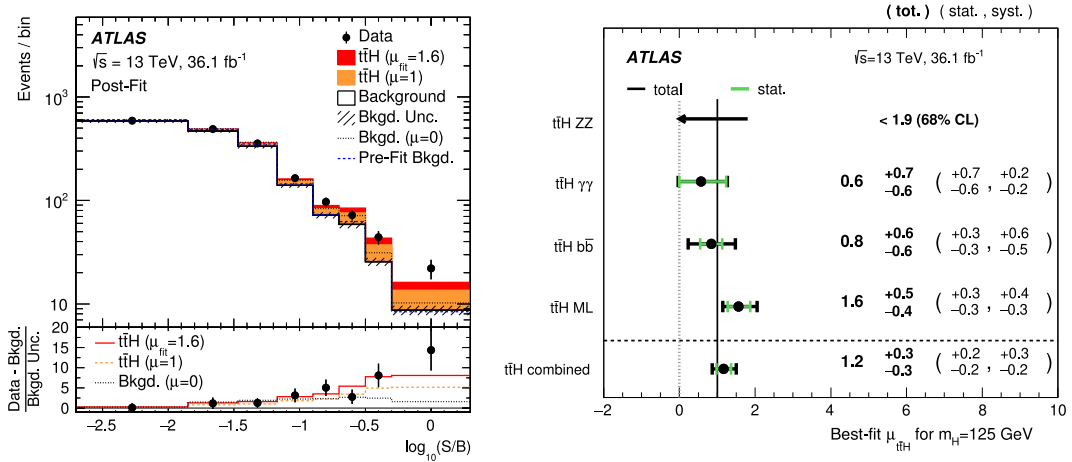
Fig. 34. Event yields as a function of $\log_{10}(Su/B)$ for data, background and a Higgs boson signal with $m_H = 125$ GeV. The discriminant bins in all signal regions are combined into bins of $\log_{10}(S/uB)$, where S is the expected signal yield and B the background yield from the unconditional fit. The signal yields are shown for the fitted value $\mu = 1.6$ and the SM prediction $\mu = 1$. The total background before the fit is shown as a dashed histogram. The pull of the data relative to the background-only prediction is shown in the lower panel, where the full line indicates the pull of the prediction for signal with $\mu = 1.6$ and background relative to the background-only prediction [76] (left). Summary of the measurements of the signal strength from individual analyses and the combined result. As no events are observed in the $H \to ZZ \to 4l$ analysis, a 68% confidence level (CL) upper limit on μ is reported [76] (right).

signal regions are combined into bins of $\log_{10}(Su/B)$, S being the expected signal yield and B the fitted background yield. The multilepton analysis ($t\bar{t}H$ ML) has been combined with others $t\bar{t}H$ analysis performed with the Run 2 data [77–79]. Fig. 34 (right) shows the measurements of the signal strengths for the individual analysis and for the combination. The observed (expected) signal significance for the combined analysis is 4.2 σ (3.8 σ). The combined signal strength $\mu = 1.2 \pm 0.3$ is compatible with the SM expectation. A similar analysis made by the CMS experiment is expected to be ready soon.

5. Higgs boson pair production and Higgs boson self-couplings

Higgs boson pair production in the SM is rare. The main production modes are the pair production through a quark loop and through the self-couplings of the Higgs boson (Fig. 35). These diagrams interfere negatively making the overall production rate smaller than what would be expected in the absence of a trilinear coupling. The Feynman diagram in Fig. 35 (left) is the off-shell $H^* \to HH$. The on-shell $H \to H^*H^*$ is strongly disfavored. The Higgs boson self-couplings are uniquely determined by the structure of the scalar potential:

$$\mathcal{L}_{\text{H-self,U-gauge}} = -\frac{M_H^2}{2v}H^3 - \frac{M_H^2}{8v^2}H^4 \qquad (92)$$

Experimentally measuring trilinear and quartic Higgs boson self-couplings is a crucial test of the mechanism of electroweak symmetry breaking. Models of physics beyond the SM with single Higgs boson and signal strengths compatible with SM can exhibit a double Higgs boson phenomenology different from the SM expectation. A deviation of the trilinear Higgs boson self-coupling from the SM value may enhance the HH production rate significantly. The searches for Higgs boson pair production has been performed by ATLAS and CMS combining the different $b\bar{b}$, $\tau^+\tau^-$, $4l$, $2l2\nu$, $\gamma\gamma$ decays for the two Higgs bosons. The double Higgs boson searches are divided into resonant and non-resonant. For non-resonant HH production, only the number of events passing the final selection is used whereas the m_{4f} distribution is used in the case of the search for HH resonances. No significant excess relative to the background has been found. Considering some recent results:

- ATLAS for HH $\to b\bar{b}b\bar{b}$ at $\sqrt{s} = 13$ TeV [80] found at 95% C.L. a non-resonant $\sigma \times BR$ upper limit 100 times the SM expectation;
- CMS combining $HH \to b\bar{b}\gamma\gamma$ at $\sqrt{s} = 8$ TeV [81] and $HH \to b\bar{b}\tau\tau$ at $\sqrt{s} = 8$ TeV [82] found at 95% C.L. a non-resonant $\sigma \times BR$ upper limit 43 times the SM expectation.

6. Higgs boson measurements at the High-Luminosity LHC

The current program of LHC is to complete the Run 2 in 2018. Two years of shutdown (LS2) will be dedicated to the Phase 1 upgrade of detectors and to the LHC upgrade required to reach the luminosity of 2×10^{34} cm^{-2} s^{-1}. The Run 3 will start in 2021 with the aim to collect 300 fb^{-1} of integrated luminosity per experiment in about three years. Another shutdown of about two years (LS3) will be dedicated to the Phase 2 upgrade of detectors and to the LHC upgrade required to reach the
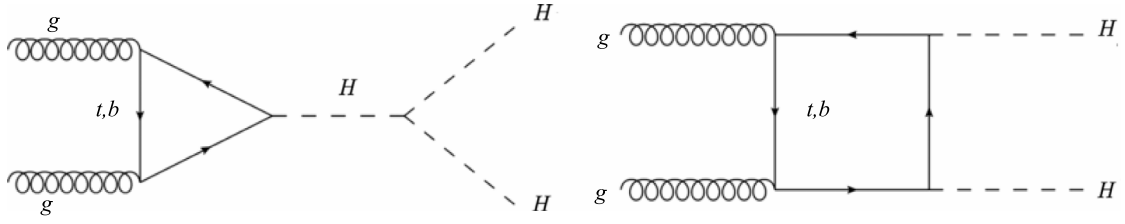
Fig. 35. Feynman diagrams contributing to Higgs boson pair production through (left) the self-couplings of the Higgs boson and (right) a top- and b-quark loop.
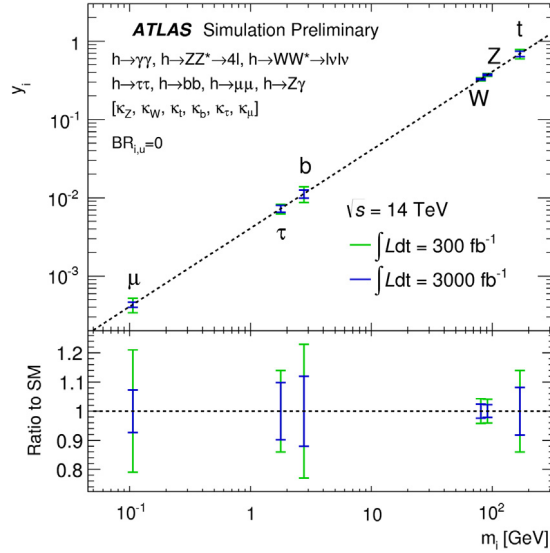

Fig. 36. Fit results for the reduced coupling scale factors y_i ($k_F m_F/v$ for fermions, and $\sqrt{k_V} m_V/v$ for vector bosons) as a function of the particle mass assuming 300 or 3000 fb^{-1} of integrated luminosity and a *SM* Higgs boson with a mass of 125 GeV [83].

luminosity of 5×10^{34} cm^{-2} s^{-1}. The High-Luminosity LHC (HL-LHC) will start in 2026 with the aim to collect 3000 fb^{-1} of integrated luminosity per experiment in about a dozen years. The ATLAS and CMS Collaborations made two independent studies to evaluate the projections of Higgs boson analysis at HL-LHC [83,84]. The ATLAS experiment generated 14 TeV events smearing the transverse momentum and energy of the reconstructed particles to take into account the upgraded detector. The CMS experiment projected the analysis performed with the 13 TeV data sample collected in 2015 and early 2016. The projections are performed under different scenarios considering the systematic uncertainties in the present and in the HL-LHC conditions. Fig. 36 shows the ATLAS projections of the reduced coupling scale factors defined in Section 4.4.7 as a function of the mass of the particle involved in the coupling. The expected precision of the coupling measurements with 3000 fb^{-1} of integrated luminosity is about 3% for the W/Z bosons, 7% for the muons, 10% for τ leptons and bottom or top type quarks. The precision of the coupling to muons is competitive to the expected precision at the CLIC collider with $\sqrt{s} = 3$ TeV. Fig. 37 show the CMS projected signal strengths inclusively and for different production modes at 3000 fb^{-1} of integrated luminosity for the $H \rightarrow \gamma\gamma$ channel (left) and for the $H \rightarrow ZZ \rightarrow 4l$ channel (right). In the scenario S1+ all systematic uncertainties are kept constant with integrated luminosity. The effects of higher pileup conditions and detector upgrades on the future performance of CMS are taken into account. In the scenario S2+ the theoretical uncertainties are scaled down by a factor 1/2, while experimental systematic uncertainties are scaled down by the square root of the integrated luminosity until they reach a defined lower limit based on estimates of the achievable accuracy with the upgraded detector. The effects of higher pileup conditions and detector upgrades on the future performance of CMS are taken into account. The projected inclusive uncertainties for the signal strengths $\mu^{\gamma\gamma}$ and μ^{ZZ} are both 8% for the S1+ scenario and 5% for the S2+ scenario.

7. The global electroweak fit

For a long time, global fits of precise measurements performed with the experiments running at the lepton and hadron colliders (LEP, SLC, Tevatron, LHC) have been used to constrain free parameters of the *SM* such as the Higgs boson and top
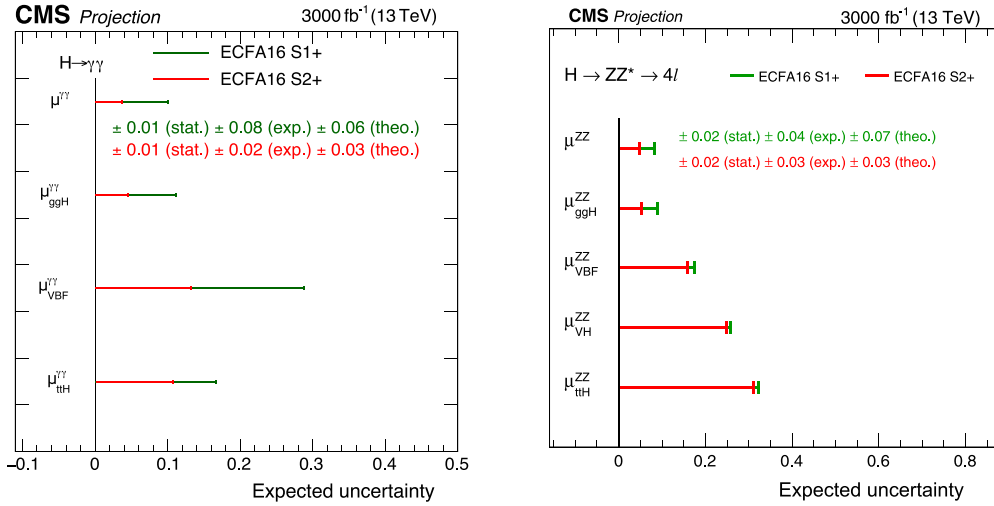
Fig. 37. Projected uncertainties for the $H \rightarrow \gamma\gamma$ (left) and $H \rightarrow ZZ \rightarrow 4l$ (right) signal strengths relative to the standard model, inclusively and per production mode. Projections are given for 3000 fb^{-1} under the scenarios described in the text [84].

quark masses. Today all the fundamental parameters entering these fits are experimentally determined, and the global fits are used as powerful tools to assess the validity of the theory and to constrain scenarios for new physics. Recently the ATLAS collaboration presented the first LHC measurement of the W mass [85] with a precision comparable with the LEP2 and Tevatron combination. The contribution of the hadron colliders to the global electroweak fits can therefore go beyond the precise measurement of the Higgs boson and top quark masses. The references of the experimental measurements reported in the first column of Table 14 can be found in [86]. The result of the fit has been presented at EPS-HEP2017 including, with respect to the previous reference, the last measurements of the top and W masses [87]. The measurements are used to fit the 5 parameters $\alpha_s(M_Z)$, $\Delta\alpha_{\mathrm{had}}^{(5)}(M_Z)$, M_Z, m_t, m_H then the pseudo-observables are determined and reported in the column *Posterior*. For every raw of Table 14 the fit is performed also by excluding the measurement in the raw, results are reported in the column *Prediction*. The *Pull* is the ratio $(O_{\mathrm{meas.}} - O_{\mathrm{pred.}})/\sigma_{\mathrm{meas.}}$. The fits have been performed using the HEPfit [88] code. All the considered measurements are compatible with the *SM* fit. The larger deviation, already present in the LEP electroweak fit, is the forward backward asymmetry for the b-tagged quarks.

Some experimental measurements like the muon anomalous magnetic moment from the Muon g-2 Collaboration [89], the angular distributions of the $B \rightarrow K^*l^+l^-$ decay or the test of lepton universality with the decay ratio $R_{K*0} = \frac{BR(B^0 \rightarrow K^{*0}\mu^+\mu^-)}{BR(B^0 \rightarrow K^{*0}J/\psi(\rightarrow \mu^+\mu^-))} / \frac{BR(B^0 \rightarrow K^{*0}e^+e^-)}{BR(B^0 \rightarrow K^{*0}J/\psi(\rightarrow e^+e^-))}$ from the LHCb and Belle Collaborations [90–92] show discrepancies with respect to the *SM* expectation of about 3σ. More precise measurements from the LHC, Belle II or new experiments will help to clarify if they are a statistical fluctuation or hint at a new era of physics.

8. The extended Higgs sectors and the new physics

This review is intended to introduce the Standard Model theory with a minimal Higgs field doublet, to describe the historical Higgs boson searches, the recent measurements of the Standard Model Higgs boson and the physics perspectives at the future colliders. Readers interested in the extended Higgs sector and in physics beyond the Standard Model can find interesting recent reviews:

- "Higgs boson production and decay at hadron colliders" [17] where the Minimal Supersymmetric Extension is considered in addition to the SM;
- "Building and testing models with extended Higgs sectors" [93] where the extended Higgs sector with multiple Higgs field doublets is discussed in depth;
- "Experimental status of supersymmetry after the LHC Run-I" [94];
- "LHC searches for exotic new particles" [95].

9. Conclusions

The SLD, LEP, Tevatron and other experiments provided several important measurements of Standard Model observables like the forward backward asymmetries, the Z and W bosons masses and widths, the Weinberg angle and the top quark

Table 14

Experimental measurement, posterior, prediction, and pull for the 5 input parameters ($\alpha_s(M_Z)$, $\Delta\alpha_{\text{had}}^{(5)}(M_Z)$, M_Z, m_t, m_H), and for the main pseudo-observables considered in the *SM* fit [86]. The values in the column *Prediction* are determined without using the experimental information for the corresponding observable.

	Measurement	Posterior	Prediction	Pull
$\alpha_s(M_Z)$	0.1180 ± 0.0010	0.1180 ± 0.0009	0.1184 ± 0.0028	-0.1
$\Delta\alpha_{\text{had}}^{(5)}(M_Z)$	0.02750 ± 0.00033	0.02743 ± 0.00025	0.02734 ± 0.00037	0.3
M_Z [GeV]	91.1875 ± 0.0021	91.1880 ± 0.0021	91.198 ± 0.010	-1.0
m_t [GeV]	$173.1 \pm 0.6 \pm 0.5$	173.43 ± 0.74	176.1 ± 2.2	-1.3
m_H [GeV]	125.09 ± 0.24	125.09 ± 0.24	100.6 ± 23.6	1.0
M_W [GeV]	80.379 ± 0.012	80.3643 ± 0.0058	80.3597 ± 0.0067	1.4
Γ_W [GeV]	2.085 ± 0.042	2.08873 ± 0.00059	2.08873 ± 0.00059	-0.1
$\sin^2\theta_{\text{eff}}^{\text{lept}}(Q_{\text{FB}}^{\text{had}})$	0.2324 ± 0.0012	0.231454 ± 0.000084	0.231449 ± 0.000085	0.8
$P_\tau^{\text{pol}} = A_\ell$	0.1465 ± 0.0033	0.14756 ± 0.00066	0.14761 ± 0.00067	-0.3
Γ_Z [GeV]	2.4952 ± 0.0023	2.49424 ± 0.00056	2.49412 ± 0.00059	0.5
σ_h^0 [nb]	41.540 ± 0.037	41.4898 ± 0.0050	41.4904 ± 0.0053	1.3
R_ℓ^0	20.767 ± 0.025	20.7492 ± 0.0060	20.7482 ± 0.0064	0.7
$A_{\text{FB}}^{0,\ell}$	0.0171 ± 0.0010	0.01633 ± 0.00015	0.01630 ± 0.00015	0.8
A_ℓ (SLD)	0.1513 ± 0.0021	0.14756 ± 0.00066	0.14774 ± 0.00074	1.6
R_b^0	0.21629 ± 0.00066	0.215795 ± 0.000027	0.215793 ± 0.000027	0.7
R_c^0	0.1721 ± 0.0030	0.172228 ± 0.000020	0.172229 ± 0.000021	-0.05
$A_{\text{FB}}^{0,b}$	0.0992 ± 0.0016	0.10345 ± 0.00047	0.10358 ± 0.00052	-2.6
$A_{\text{FB}}^{0,c}$	0.0707 ± 0.0035	0.07394 ± 0.00036	0.07404 ± 0.00040	-0.9
A_b	0.923 ± 0.020	0.934787 ± 0.000054	0.934802 ± 0.000061	-0.6
A_c	0.670 ± 0.027	0.66813 ± 0.00029	0.66821 ± 0.00032	0.1
$\sin^2\theta_{\text{eff}}^{\text{lept}}$(Tev/LHC)	0.23166 ± 0.00032	0.231454 ± 0.000084	0.231438 ± 0.000087	0.7

mass with a precision up to 10^{-5}. At the end of the LEP and Tevatron data taking, no relevant discrepancies with respect to the Standard Model expectations have been observed and the Higgs boson mass has been constrained between 114 and 149 GeV (or over 182 GeV) at 95% C.L. After 48 years from the postulate of an elementary scalar boson, the discovery of a new neutral boson in the search for the *SM* Higgs boson at the LHC has been reported on July 4th 2012. The data collected by ATLAS and CMS in the Run 1 provided the first information about the new particle. The mass of the new boson has been measured to be near 125 GeV with a precision of 1.9‰. The spin-parity state $J^P = 0^+$ is strongly favored, considering the most conservative measurement the confidence level is 99.95% with respect to the 0^- state, 99.97% with respect to the 1^+ state, 99.73% with respect to the 1^- state. The signal strengths and the coupling modifiers have been measured with a precision of 20% or lower and they are compatible with 1 that means the Higgs boson couplings are compatible with the *SM* expectations. The Run 2 and the following LHC high luminosity program have the goal to search the evidence of new physics signals and to characterize the Standard Model and the Higgs boson with the highest possible precision. The future electron–positron colliders have the potential to measure many couplings with a precision better than 2% and to measure the Higgs boson width with a precision of 3.5% and the Higgs boson mass with a precision of 0.24‰. The current predictions of the global electroweak fit are compatible with the experimental measurements. New precise measurements will help to clarify the origin of the current discrepancies in the B-sector and of the muon anomalous magnetic moment.

Acknowledgments

References

[1] A.H. Becquerel, C. R. Acad. Sci. Paris 122 (1896) 420.
[2] W. Pauli, Letter to the Physical Society of Tuebingen, December 4, 1930, American Physical Society Meeting in Pasadena, June 1931.

[3] J. Chadwick, Nature 129 (1932) 312.
[4] E. Fermi, Nuovo Cimento 11 (1934) 1.
[5] J. Schwinger, Ann. Phys., NY 2 (1957) 407.
[6] S.A. Bludman, Nuovo Cimento 9 (1958) 433.
[7] S.L. Glashow, Nuclear Phys. 22 (1961) 579.
[8] S. Weinberg, Phys. Rev. Lett. 19 (1967) 1264.
[9] A. Salam, Elementary Particle Theory, Almqvist and Wiksells, Stockholm, 1969, p. 36.
[10] I. Aitchison, A. Hey, Gauge Theories in Particle Physics, Adam Hilger, Bristol, UK, 1982.
[11] C. Quigg, Gauge Theories of the Strong, Weak, and Electromagnetic Interactions, Benjamin-Cummings, Reading, USA, 1983.
[12] F. Halzen, A.D. Martin, Quarks and Leptons: An Introductory Course in Modern Particle Physics, Wiley, New York, USA, 1984.
[13] M.E. Peskin, D.V. Schroeder, An Introduction to Quantum Field Theory, Addison-Wesley, Reading, USA, 1995.
[14] S. Dittmaier, M. Schumacher, Prog. Part. Nucl. Phys. 70 (2013) 1.
[15] A. Nisati, G. Tonelli, Riv. Nuovo Cimento 38 (11) (2015) 507.
[16] P. Checchia, Internat. J. Modern Phys. A 30 (2015) 153003.
[17] M. Spira, Prog. Part. Nucl. Phys. 95 (2017) 98.
[18] M. Gell-Mann, Phys. Lett. 8 (1964) 214.
[19] G. Zweig, An SU3 Model for Strong Interaction Symmetry and Its Breaking, CERN-Report 8182/TH401, 1964.
[20] J. Goldstone, Nuovo Cimento 19 (1961) 154.
[21] J. Goldstone, A. Salam, S. Weinberg, Phys. Rev. 127 (1962) 965.
[22] F. Englert, R. Brout, Phys. Rev. Lett. 13 (1964) 321.
[23] P.W. Higgs, Phys. Lett. 12 (1964) 132.
[24] P.W. Higgs, Phys. Rev. Lett. 13 (1964) 508.
[25] G.S. Guralnik, C.R. Hagen, T.W.B. Kibble, Phys. Rev. Lett. 13 (1964) 585.
[26] M.L. Mangano, et al., J. High Energy Phys. 0307 (2003) 001.
[27] J. Alwall, et al., The automated computation of tree-level and next-to-leading order differential cross sections, and their matching to parton shower simulations, 2014. arXiv:1405.0301 [hep-ph].
[28] S. Frixione, F. Stoeckli, P. Torrielli, B.R. Webber, C.D. White, The MCaNLO 4.0 Event Generator, 2010 arXiv:1010.0819 [hep-ph].
[29] S. Frixione, P. Nason, C. Oleari, J. High Energy Phys. 0711 (2007) 070.
[30] T. Gleisberg, et al., J. High Energy Phys. 0902 (2009) 007.
[31] W. Kilian, T. Ohl, J. Reuter, Eur. Phys. J. C 71 (2011) 1742.
[32] T. Sjöstrand, et al., Comput. Phys. Comm. 191 (2015) 159.
[33] J. Bellm, et al., Eur. Phys. J. C 76 (2016) 196.
[34] A. Alloul, N.D. Christensen, C. Degrande, C. Duhr, B. Fuks, Comput. Phys. Comm. 185 (2014) 2250.
[35] Wolfram Research, Inc. Mathematica, Version 11.1, Champaign, IL, 2017.
[36] S. Weinberg, Phys. Rev. 133 (1964) B1318.
[37] LHC Higgs Cross Section Working Group, D. de Florian, C. Grojean, F. Maltoni, C. Mariotti, A. Nikitenko, M. Pieri, P. Savard, M. Schumacher, R. Tanaka (Eds.), Handbook of LHC Higgs Cross Sections: 4. Deciphering the Nature of the Higgs Sector, CERN-2017-002-M, CERN, Geneva, 2017. arXiv:1610.07922v2 [hep-ph].
[38] LHC Higgs Cross Section Working Group, S. Heinemeyer, C. Mariotti, G. Passarino, and R. Tanaka (Eds.), Handbook of LHC Higgs Cross Sections: 3. Higgs Properties, CERN-2013-004, CERN, Geneva, 2013, arXiv:1307.1347 [hep-ph].
[39] H. Abramowicz, et al., Eur. Phys. J. C 77 (2017) 475.
[40] ALEPH Collaboration, DELPHI Collaboration, L3 Collaboration, OPAL Collaboration, LEP Working Group, Phys. Lett. B 565 (2003) 61.
[41] The CEPC-SPPC Study Group, CEPC-SPPC Progress Report (2015–2016), IHEP-CEPC-DR-2017-01.
[42] D.M. Asner, et al., ILC Higgs White Paper, 2013 arXiv:1310.0763 [hep-ph].
[43] K. Fujii, et al., Physics Case for the International Linear Collider, 2015 arXiv:150605992 [hep-ex].
[44] U. Aglietti, et al., Tevatron-for-LHC Report: Higgs, 2007 arXiv:hep-ph/0612172v2.
[45] F. Cascioli, et al., Phys. Lett. B 735 (2014) 311.
[46] T. Gehrmann, et al., Phys. Rev. Lett. 113 (2014) 212001.
[47] CDF Collaboration and D0 Collaboration, Phys. Rev. D 88 (2013) 052014.
[48] S. Chatrchyan, et al. [CMS Collaboration], Phys. Lett. B 710 (2012) 26.
[49] G. Aad, et al. [ATLAS Collaboration], Phys. Rev. D 86 (2012) 032003.
[50] G. Aad, et al. [ATLAS Collaboration], Phys. Lett. B 716 (2012) 1.
[51] S. Chatrchyan, et al. [CMS Collaboration], Phys. Lett. B 716 (2012) 30.
[52] G. Aad, et al. [ATLAS and CMS Collaborations], Phys. Rev. Lett. 114 (2015) 191803.
[53] S.Y. Choi, D.J. Miller, M.M. Mühlleitner, P.M. Zerwas, Phys. Lett. B 553 (2003) 61.
[54] M.M. Mühlleitner, Determination of Higgs Spin and Parity At the LHC, INSPIRE-1268433, 2013.
[55] S. Bolognesi, Y. Gao, A.V. Gritsan, K. Melnikov, M. Schulze, N.V. Tran, A. Whitbeck, Phys. Rev. D 86 (2012) 095031.
[56] G. Aad, et al. [ATLAS Collaboration], Eur. Phys. J. C 75 (2015) 476.
[57] S. Chatrchyan, et al. [CMS Collaboration], Phys. Rev. D 89 (2014) 092007.
[58] V. Khachatryan, et al. [CMS Collaboration], Phys. Rev. D 92 (2015) 012004.
[59] G. Aad, et al. [ATLAS Collaboration], Phys. Lett. B 726 (2013) 120.
[60] V. Khachatryan, et al. [CMS Collaboration], Phys. Rev. D 92 (2015) 032008.
[61] G. Aad, et al. [ATLAS and CMS Collaborations], J. High Energy Phys. 08 (2016) 045.
[62] J. Ellis, T.J. You, J. High Energy Phys. 06 (2013) 103.
[63] G. Aad, et al. [ATLAS Collaboration], Eur. Phys. J. C 75 (2015) 335.
[64] V. Khachatryan, et al. [CMS Collaboration], J. High Energy Phys. 1609 (2016) 051.
[65] M. Aaboud, et al. [ATLAS Collaboration], J. High Energy Phys. 1710 (2017) 132.
[66] ATLAS CONF Note [ATLAS Collaboration], Measurement of the Higgs boson mass in the $H \rightarrow ZZ^* \rightarrow 4\ell$ and $H \rightarrow \gamma\gamma$ channels with $\sqrt{s} = 13$ TeV pp collisions using the ATLAS detector, ATLAS-CONF-2017-046, 2017.
[67] ATLAS CONF Note [ATLAS Collaboration], Combined measurements of Higgs boson production and decay in the $H \rightarrow ZZ^* \rightarrow 4\ell$ and $H \rightarrow \gamma\gamma$ channels using $\sqrt{s} = 13$ TeV pp collision data collected with the ATLAS experiment, ATLAS-CONF-2017-047, 2017.
[68] CMS PAS Note [CMS Collaboration], Measurements of properties of the Higgs boson in the diphoton decay channel with the full 2016 data set, CMS-PAS-HIG-16-040, 2017.
[69] A.M. Sirunyan, et al. [CMS Collaboration], J. High Energy Phys. 1711 (2017) 047.

[70] G. Aad, et al. [ATLAS Collaboration], Phys. Rev. D 91 (2015) 012006.
[71] G. Aad, et al. [ATLAS Collaboration], Phys. Rev. D 90 (2014) 052004.
[72] V. Khachatryan, et al. [CMS Collaboration], Eur. Phys. J. C 74 (2014) 3076.
[73] A.M. Sirunyan, et al. [CMS Collaboration], Observation of the Higgs Boson Decay to Pair of Tau Leptons, CERN-EP-2017-181, 2017 arXiv:1708.00373 [hep-ex].
[74] M. Aaboud, et al. [ATLAS Collaboration], J. High Energy Phys. 12 (2017) 024.
[75] A.M. Sirunyan, et al. [CMS Collaboration], Evidence for the Higgs Boson Decay to a Bottom Quark–Antiquark Pair, CERN-EP-2017-233, 2017 arXiv: 1709.07497 [hep-ex].
[76] M. Aaboud, et al. [ATLAS Collaboration], Evidence for the Associated Production of the Higgs Boson and a Top Quark Pair with the ATLAS Detector, CERN-EP-2017-281, 2017 arXiv:1712.08891.
[77] M. Aaboud, et al. [ATLAS Collaboration], Search for the Standard Model Higgs Boson Produced in Association with Top Quarks and Decaying Into a $B\bar{B}$ Pair in Pp Collisions At $\sqrt{S}$, 2017 arXiv:1712.08895.
[78] Measurement of the $t\bar{t}$ production cross section in the τ + jets final state in pp collisions at $\sqrt{s} = 8$ TeV using the ATLAS detector, CERN-EP-2017-288, 2017. arXiv:1702.08839.
[79] M. Aaboud, et al. [ATLAS Collaboration], Measurement of the Higgs Boson Coupling Properties in the $H \rightarrow ZZ^* \rightarrow 4\ell$ Decay Channel At $\sqrt{s} = 13$ TeV with the ATLAS detector, CERN-EP-2017-206, 2017 arXiv:1712.02304.
[80] M. Aaboud, et al. [ATLAS Collaboration], Phys. Rev. D 94 (2016) 052002.
[81] V. Khachatryan, et al. [CMS Collaboration], Phys. Rev. D 94 (2016) 052012.
[82] A.M. Sirunyan, et al. [CMS Collaboration], Phys. Rev. D 96 (2017) 072004.
[83] ATLAS PUB Note, Projections for measurements of Higgs boson signal strengths and coupling parameters with the ATLAS detector at the HL-LHC, ATL-PHYS-PUB-2014-016.
[84] CMS PAS Note, Projected performance of Higgs analyses at the HL-LHC for ECFA 2016, CMS PAS FTR-16-002.
[85] M. Aaboud, et al. [ATLAS Collaboration], Measurement of the W-Boson Mass in PP Collisions at $\sqrt{s} = 7$ TeV with the ATLAS Detector, CERN-EP-2016-305, 2017 arXiv:1701.07240.
[86] J. de Blas, M. Ciuchini, E. Franco, S. Mishima, M. Pierini, L. Reina, L. Silvestrini, J. High Energy Phys. 1612 (2016) 135.
[87] J. de Blas, M. Ciuchini, E. Franco, S. Mishima, M. Pierini, L. Reina, L. Silvestrini, The Global Electroweak and Higgs Fits in the LHC Era, 2017 arXiv: 1710.05402 [hep-ph].
[88] HEPfit Collaboration, http://hepfit.roma1.infn.it.
[89] G.W. Bennett, et al. [Muon g-2 Collaboration], Phys. Rev. D 73 (2006) 072003.
[90] R. Aaij, et al. [LHCb Collaboration], J. High Energy Phys. 1602 (2016) 104.
[91] S. Wehle, et al. [Belle Collaboration], Phys. Rev. Lett. 118 (2017) 111801.
[92] R. Aaij, et al. [LHCb Collaboration], J. High Energy Phys. 08 (2017) 055.
[93] I.P. Ivanov, Prog. Part. Nucl. Phys. 95 (2017) 160.
[94] C. Autermann, Prog. Part. Nucl. Phys. 90 (2016) 125.
[95] T. Golling, Prog. Part. Nucl. Phys. 90 (2016) 156.